Mixed bottom-friction–Kelvin–Helmholtz destabilization of source-driven abyssal overflows in the ocean

GORDON E. SWATERS†

Applied Mathematics Institute, Department of Mathematical & Statistical Sciences
and
Institute for Geophysical Research, University of Alberta, Edmonton, AB T6G 2G1, Canada

Source-driven ocean currents that flow over topographic sills are important initiation sites for the abyssal component of the thermohaline circulation. These overflows exhibit vigorous space and time variability over many scales as they progress from a predominately gravity-driven downslope flow to a geostrophic along-slope current. Observations show that in the immediate vicinity of a sill, grounded abyssal ocean overflows can possess current speeds greater than the local long internal gravity wave speed with bottom friction and downslope gravitational acceleration dominating the flow evolution. It is shown that these dynamics lead to the mixed frictionally induced and Kelvin–Helmholtz instability of grounded abyssal overflows. Within the overflow, the linearized instabilities correspond to bottom-intensified baroclinic roll waves, and in the overlying water column amplifying internal gravity waves are generated. The stability characteristics are described as functions of the bottom drag coefficient and slope, Froude, bulk Richardson and Reynolds numbers associated with the overflow and the fractional thickness of the abyssal current compared to the mean depth of the overlying water column. The marginal stability boundary and the boundary separating the parameter regimes in which the most unstable mode has a finite or infinite wavenumber are determined. When it exists, the high-wavenumber cutoff is obtained. Conditions for the possible development of an ultraviolet catastrophe are determined. In the infinite-Reynolds-number limit, an exact solution is obtained which fully includes the effects of mean depth variations in the overlying water column associated with a sloping bottom. For parameter values characteristic of the Denmark Strait overflow, the most unstable mode has a wavelength of about 19 km, a geostationary period of about 14 hours, an e-folding amplification time of about 2 hours and a downslope phase speed of about 74 cm s^{-1}.

1. Introduction

The flow of grounded dense water over deep sills is a source point for the initiation of abyssal ocean currents. These flows, such as the Denmark Strait overflow (DSO; see e.g. Worthington 1969; Dickson & Brown 1994; Käse & Oschlies 2000; Girton & Sanford 2001, 2003; Jungclaus, Jauser & Käse 2001, among many others), make an important global-scale contribution to the convective overturing of the oceans. Density-driven grounded currents are responsible, as well, for deepwater replacement

† Email address for correspondence: gordon.swaters@ualberta.ca

in marginal seas (e.g. LeBlond *et al.* 1991; Karsten, Swaters & Thomson 1995; Masson 2002) and the along-continental slope propagation of cold, bottom-intensified anomalies (e.g. Houghton *et al.* 1982; Swaters & Flierl 1991).

Käse, Girton & Sanford (2003), analysing oceanographic data for the DSO region and high-resolution numerical simulations, described the differing dynamical regimes between the near-sill and downstream regions for grounded abyssal flow. In the downstream region, the current is more or less in geostrophic balance and flows, on average, along isobaths. The near-sill overflow is predominately downslope, strongly influenced by bottom friction and is near, and even possibly, supercritical with speeds exceeding 1 m s^{-1}. Girton & Sanford (2003) argued the near-sill momentum balance is principally between rotation, downslope gravitational acceleration and bottom friction. This structure can be qualitatively seen in figure 1(*a*) in Swaters (2006*a*), which shows the depth of the 1.8° potential temperature isotherm (contoured every 500 m) associated with DSO water as derived from Worthington & Wright (1970). This figure shows the DSO current descending the sloping bottom into the North Atlantic. In particular, the comparatively pronounced cross-isobath flow of the DSO water mass between Greenland and Iceland can be clearly seen.

There is considerable temporal and spatial variability associated with overflows (Spall & Price 1998). This variability occurs over a broad range of frequencies and wavelengths. In the sub-inertial regime, abyssal currents can be baroclinically unstable (Swaters 1991, 2006*b*; Jungclaus *et al.* 2001; Reszka, Swaters & Sutherland 2002) and can produce mesoscale eddies (Bruce 1995; Krauss & Käse 1998; Swaters 1998, 2006*c*). In the near-sill region, where the overflow speeds are quite large and geostrophy is no longer the primary dynamical balance, there can be other higher frequency sources for the transition to instability.

Cenedese *et al.* (2004) described a sequence of laboratory experiments for density-driven abyssal currents flowing down a sloping bottom in a rotating tank. Their investigation showed over a large range of flow parameters (i.e. rotation rate, density, bottom slope and the volume flux of the source) the abyssal current progressed from laminar to the emergence of 'wavelike disturbances' on the interface between the overflow and the overlying water column to the periodic formation of cyclonic eddies in the overlying water column. The experiments of Cenedese *et al.* (2004) showed the 'wave regime' is associated with the Froude number being greater than 1; i.e. the speeds within the density current exceeded the local long internal gravity wave speed. Cenedese *et al.* (2004) speculated the 'wavelike disturbances' were manifestations of a rotational analogue of a roll-wave instability.

Earlier, Baines (1984, 1995) described several laboratory experiments on the near and supercritical flow of a two-layer fluid down an incline. Lyapidevskii (2000) described the periodic discontinuous solutions (i.e. finite-amplitude roll waves) of such flows in the high-Reynolds-number limit. With respect to the transition to instability in the oceanographically relevant context, Swaters (2003, 2006*a*) has shown in the near-inertial regime supercritical overflows can be destabilized by bottom friction even when rotation or full dynamic coupling with an ambient internal gravity wave field occurs. Within the overflow, the instabilities take the form of propagating, growing periodic bores or pulses (and are the rotational mesoscale analogues of classical roll waves). In the overlying water column the instabilities take the form of amplifying internal gravity waves.

For typical DSO parameter values and in a dynamical regime in which there is, to the leading order, no dynamical feedback by the internal gravity waves back upon the overflow, i.e. a classical reduced-gravity model, Swaters (2003) has shown the most

unstable mode has a wavelength about 30 km and propagates prograde with respect to the overflow with a geostationary period about 2 hours and an e-folding growth time about 24 hours. As the dynamical interaction between the unstable overflow and the gravity wave field becomes more important, e.g. a 2.5-layer model, these stability characteristics can be dramatically blue-shifted (Swaters 2006*a*) with the most unstable mode having a wavelength of about 500 m and propagating retrograde with respect to the overflow with a geostationary period of about 17 minutes and an e-folding growth time of about 13 minutes.

There remain many aspects of the dynamics of grounded abyssal overflows that are of interest. For example, the dynamical sequence from source-driven, frictionally dominated cross-isobath flow to inertial geostrophically balanced, topographically steered flow is yet to be completely described. Within that scenario, the full transition sequence from frictionally induced instability to Kelvin–Helmholtz (KH) destabilization and finally on to baroclinic instability and the associated entrainment processes awaits full clarification. Sutyrin (2007) has described the mixed KH–baroclinic instability characteristics for uniform geostrophically balanced flow along a slope. However, in the near-sill region in which frictional processes are important, the development of unstable abyssal overflows and the subsequent interaction with internal gravity waves remain incompletely understood (Käse *et al.* 2003). These processes are important not only for the interpretation of oceanographic observations and laboratory experiments but also in correctly parameterizing abyssal-layer mixing processes, particularly those involving gravity waves and bottom friction, in the present generation of ocean general circulation and climate models.

The principal purpose of this paper is to describe the stability characteristics of non-rotating baroclinic abyssal overflows in which both frictionally induced and KH instability can occur where the destabilization generates internal gravity waves in the overlying water column, which dynamically interact with the amplifying roll waves in the abyssal current. A comment on the title of this paper is in order. The use of the word 'mixed' in reference to the instability mechanism is not meant to imply that both bottom friction and vertical velocity shear must be present for abyssal overflows to become unstable. Rather, for typical parameter regimes characteristic of oceanic abyssal overflows in the 'near-sill' region both frictional and Kelvin–Helmholtz destabilization can occur simultaneously. Depending on where precisely the flow exists in parameter space one or the other of the instability mechanisms may dominate. The goal of this paper is to describe the stability characteristics of abyssal overflows when both of these instability mechanisms is occurring – over the full range of plausible oceanographic parameters.

The outline of this paper is as follows. In §2, the model geometry and non-dimensional equations are introduced; parameter estimates are given; and the linear stability problem is derived. In §3, the linear stability characteristics are determined in the finite-Reynolds-number limit when the mean depth variations associated with the sloping bottom can be neglected in the overlying water column. In §4, the linear stability characteristics are described when the bottom slope cannot be neglected in the upper layer in the high-Reynolds-number approximation. The paper is summarized in §5.

2. Governing equations

Motivated by the stratification characteristics in the near-sill region of the DSO (see figure 5 in Girton & Sanford 2001 as well as the abyssal model introduce by Spall
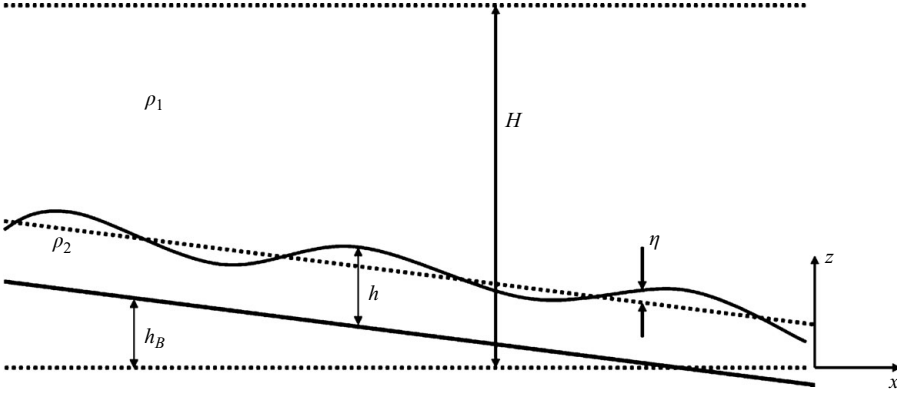
FIGURE 1. Geometry of the model used in this paper.

& Price 1998), Swaters (2006*a*) introduced a non-rotating, stably stratified shallow-water model with quadratic bottom and turbulent horizontal friction and variable topography to examine the higher frequency dynamic coupling between overflows and internal gravity waves in the overlying water column. Under a Boussinesq and rigid-lid approximation, the dimensional equations of motion for a source-driven, baroclinic abyssal current can be written in the form (see figure 1), for the upper layer,

$$(\partial_{t^*} + u_1^*\partial_{x^*})u_1^* = -\frac{1}{\rho_2}\partial_{x^*}p_1^* + A_H\partial_{x^*x^*}u_1^*, \tag{2.1}$$

$$-h_{t^*}^* + [(H - h^* - h_B^*)u_1^*]_{x^*} = 0, \tag{2.2}$$

and, for the abyssal layer,

$$(\partial_{t^*} + u_2^*\partial_{x^*})u_2^* = -\frac{1}{\rho_2}\partial_{x^*}p_2^* + A_H\frac{\partial_{x^*}(h^*\partial_{x^*}u_2^*)}{h^*} - c_D^*\frac{|u_2^*|u_2^*}{h^*} + Q^*, \tag{2.3}$$

$$h_{t^*}^* + (h^*u_2^*)_{x^*} = 0, \tag{2.4}$$

with pressure continuity given by

$$p_2^* = p_1^* + \rho_2 g'(h^* + h_B^*), \tag{2.5}$$

where $u_{1,2}^*$, $p_{1,2}^*$ and h^* are, respectively, the upper and abyssal layer horizontal velocities in the downslope (positive x^*) direction (with the subscripts 1 and 2 indicating an upper and and abyssal layer variable, respectively), the reduced upper and abyssal layer pressures and the abyssal layer thickness relative to the height of the bottom topography h_B^* which is measured positively upward, and t^* is time. The scale depth of the entire water column is H (see figure 1); $g' \equiv g(\rho_2 - \rho_2)/\rho_2 > 0$ is the reduced gravity; c_D^* is the 'unscaled' but nevertheless non-dimensional bottom friction coefficient; and A_H is the turbulent eddy viscosity, which is assumed for convenience to be the same in both layers. The abyssal current momentum source term is given by $Q^* = Q^*(x^*, t^*)$. The introduction of the rigid-lid approximation into (2.2) filters out the higher frequency 'barotropic' internal gravity waves in the upper layer and focuses attention on the relatively low-frequency internal gravity waves generated on the interface between the upper and abyssal layers. Alphabetical superscripts, unless otherwise indicated, imply partial differentiation.

Further progress is facilitated by non-dimensionalizing the governing equations. The approach adopted is to introduce a straightforward scaling based on the

internal gravity wave solutions of the model in the linearized inviscid unforced limit $A_H = c_D^* = Q^* = 0$ (see, e.g., §16 in LeBlond & Mysak 1978). That is the introduction of

$$u_1^* = [h_* U/(H - h_*)] \, u_1, p_1^* = [\rho_2 \gamma U h_*/(H - h_*)] \, p_1, u_2^* = U \, u_2, \qquad (2.6)$$

$$p_2^* = \rho_2(g'h_* + \gamma U \, p_2), h^* = h_*(1 + F\eta), h_B^* = s_* L \, h_B, x^* = L \, x, t^* = (L/\gamma) \, t, \qquad (2.7)$$

$$Q^* = (U\gamma/L) \, Q, F \equiv U/\gamma, \gamma \equiv \sqrt{g'h_*(H - h_*)/H}, \qquad (2.8)$$

where the quantities that do have not have an asterisk are non-dimensional, F is the Froude number, γ is the speed of the non-dispersive internal gravity waves in the $A_H = c_D^* = Q^* = 0$ limit, h_* is the abyssal layer thickness scale, η is the non-dimensional deviation of the abyssal layer thickness from the scale thickness (note $\eta = 0$ does not correspond to a geopotential; see figure 1); s_* is a scaling for the non-dimensional bottom slope and L and U are arbitrary length and abyssal layer velocity scales, respectively, leads to the non-dimensional equations

$$\left(\partial_t + \frac{\delta F u_1}{1 - \delta} \partial_x \right) u_1 = -\partial_x p_1 + \frac{1}{R_E} \partial_{xx} u_1, \qquad (2.9)$$

$$-\eta_t + \left[\left(1 - \frac{\delta F \eta}{1 - \delta} - s h_B \right) u_1 \right]_x = 0 \qquad (2.10)$$

and, for the abyssal layer,

$$(\partial_t + F u_2 \partial_x) u_2 = -\partial_x p_2 + \frac{\partial_x[(1 + F\eta) \, \partial_x u_2]}{R_E(1 + F\eta)} - \frac{c_D |u_2| u_2}{(1 - \delta)(1 + F\eta)F} + Q, \qquad (2.11)$$

$$\eta_t + [(1 + F\eta)u_2]_x = 0, \qquad (2.12)$$

with pressure continuity given by

$$p_2 = \frac{s h_B}{\delta F} + \frac{\eta + \delta p_1}{1 - \delta}, \qquad (2.13)$$

where the depth ratio δ, scaled bottom friction coefficient c_D, scaled slope parameter s and Reynolds number R_E are given by, respectively,

$$\delta \equiv h_*/H, c_D \equiv c_D^* L U^2/(g'h_*^2), s = s_* L/(H - h_*), R_E \equiv \gamma L/A_H. \qquad (2.14)$$

Note that necessarily $0 \leqslant \delta < 1$ (see figure 1). The equivalent-barotropic limit $H \to \infty \Longrightarrow \delta \to 0$ (with $s/\delta \to s_* L/h_*$ as $H \to \infty$) in (2.11)–(2.13) with no upper layer dynamics corresponds to the classical St. Venant model for turbulent stream flow and roll waves (Balmforth & Mandre 2004).

Oceanographically relevant estimates for the order of magnitudes of the parameters are about (see, e.g., Jiang & Garwood 1996; Spall & Price 1998; Girton & Sanford 2001, 2003; Jungclaus et al. 2001; Käse et al. 2003)

$$\left. \begin{array}{l} c_D^* \approx 0.005, H \approx 800 \, \text{m}, A_H \approx 25 \, \text{m}^2 \, \text{s}^{-1}, U \approx 1 \, \text{ms}^{-1}, \\ g' \approx 7.2 \times 10^{-4} \, \text{ms}^{-2}, h_* \approx 300 \, \text{m}, s_* \approx 0.02. \end{array} \right\} \qquad (2.15)$$

In turn, these would imply

$$\gamma \approx 37 \, \text{cms}^{-1}, \delta \approx 0.38 \text{ and } F \approx 2.7, \qquad (2.16)$$

which highlights the potential supercriticality of these overflows.

Providing a numerical estimate for c_D, s and R_E requires a specific length scale L. For example, choosing $L = l_s \equiv h_*/s_* \simeq 15$ km (implying $T \equiv l_s/\gamma \simeq 11$ hours), which

is the length scale associated with the topographic slope (Swaters 2003, 2006*a*), leads to $s \approx 0.4$, $c_D \approx 1.1$ and $R_E \approx 225$. There are other choices for the length scale that can be made (reflecting, of course, the dominant physics). For example, a shorter length scale that is important in determining the high-wavenumber cutoff in §3.1.5 arises from balancing horizontal dissipation with bottom friction in the the abyssal layer, denoted by l_D, given by

$$\frac{c_D}{(1-\delta)F} = \frac{1}{R_E} \implies L = l_D \equiv \sqrt{A_H h_*/(c_D^* U)} \simeq 1225 \, \text{m},$$

(implying $T \equiv l_D/\gamma \simeq 55$ minutes). This choice would yield $s \approx 0.05$, $c_D \approx 0.1$ and $R_E \approx 18$.

The steady downslope abyssal flow solutions which perhaps have genuine oceanographic relevance (Girton & Sanford 2003) in the near-sill region are the uniform height and velocity, i.e. 'slab', solutions (see, e.g., Jeffreys 1925; Whitham 1974; Baines 1995) given by

$$u_1 = p_1 = \eta = 0, u_2 = 1, p_2 = s h_B/(\delta F), \tag{2.17}$$

on the linearly sloping bottom

$$h_B = -x, \tag{2.18}$$

where

$$(1-\delta)FQ = s(1-\delta)/\delta - c_D. \tag{2.19}$$

These uniform flows are equivalent to the 'stream tube' solutions, without along-stream variation, which have been used to examine aspects of the dynamics of rotating turbidity and abyssal currents (e.g. Smith 1975; Killworth 1977; Price & Baringer 1994; Emms 1998). A complete discussion of the possible steady solutions for the unforced St. Venant model with more general topographic profiles has been given by Balmforth & Mandre (2004).

If $Q = 0$, then the steady 'slab' solutions must satisfy

$$\delta c_D = (1-\delta)s \iff U^2 = g's_*h_*/c_D^*, \tag{2.20}$$

which is undefined as $c_D^* \to 0$. The solution for U given by (2.20) is the frictional downslope velocity upon which classical roll-wave theory is developed (see, e.g., Jeffreys 1925; Whitham 1974; Baines 1995). The introduction of the source term Q^* provides a momentum balance so that the mean or background abyssal flow solution does not become unbounded as $c_D^* \to 0$ (which seems more physically plausible in the oceanographic context). In turn, this allows the examination of the stability characteristics in the low-bottom-drag limit in which it is expected Kelvin–Helmholtz destabilization will dominate. Similarly, under the flat bottom $s = 0$ approximation, a momentum source is required to balance the bottom drag term for a non-zero steady state to develop. Finally, of course, in the absence of a momentum source with no bottom friction on a flat bottom (i.e. $s = Q = c_D = 0$ with $\delta \neq 0$) *any* constant baroclinically sheared flow U is a steady solution (with only KH instability possible). In what follows it is assumed the current corresponds to a downslope flow, i.e. $U \geqslant 0$.

It is not possible to give an unambiguous physical interpretation for the momentum source term Q. One interpretation is that it is a parameterization for interlayer fluxes within the context of shallow-water theory similar to that introduced by Dewar (1987) for warm core rings and Swaters (2006*b*) for buoyancy-driven abyssal currents. But there are problems with that interpretation related to volume conservation (see Swaters 2006*a* for a more complete discussion). Alternatively, it may be possible to

interpret Q as crudely modelling the source associated with the release of dense water over a submerged sill; i.e. within the context of shallow-water theory Q models the 'lock release' mechanism.

From the perspective of the stability analysis presented here, however, it is important to appreciate that the momentum source term Q is not present in the stability equations, and its explicit characterization is not necessary. As is well understood, the stability properties of basic flows that are not exact solutions of the unforced governing equations may nevertheless be rationally analysed using the unforced stability equations 'without the need to consider explicitly the forces required to produce the basic state' (Pedlosky 1987 § 7.13). This is precisely the conceptual frame work required for understanding, for example, the baroclinic instability of non-zonal flow on the β-plane within the context of the quasi-geostrophic equations.

The stability theory presented here, unlike that described in Swaters (2006a), is applicable to flows for which the bottom drag coefficient c_D is zero and/or the bottom slope s is zero. In Swaters (2006a) the mean abyssal flow possessed an infinite velocity in the limit $c_D \to 0$, and in the limit $s \to 0$, there were no mean flow solutions allowed at all. Both these properties seem unphysical. In addition, Swaters (2006a) allows a 'free surface' on the upper layer, and here a rigid-upper-boundary condition is assumed. While the additional gravity wave modes allowed in Swaters (2006a) might be considered more desirable, they introduce sufficient additional complexity into the dispersion relation that a thorough theoretical analysis and the construction of detailed stability diagrams was not possible to the degree that it can be given here. Finally, with the rigid-lid approximation for the upper layer assumed here, it is possible to obtain an exact solution (see §4) to the linear stability equations with a sloping bottom in the infinite-Reynolds-number limit, which is not possible for the Swaters (2006a) model.

Substitution of

$$(u_1, \ p_1, \ \eta, \ u_2, \ p_2) = (\widetilde{u}_1, \ \widetilde{p}_1, \ \widetilde{\eta}, \ 1 + \widetilde{u}_2, \ s h_B / (\delta F) + \widetilde{p}_2),$$

into (2.9) through to (2.13), where h_B is given by (2.18) and (2.19) is assumed to hold, leads to the nonlinear perturbation equations, after dropping the tildes,

$$\left(\partial_t - R_E^{-1} \partial_{xx}\right) u_1 + \partial_x p_1 = - \left[\delta F / (1 - \delta)\right] u_1 \partial_x u_1, \tag{2.21}$$

$$\eta_t - [(1 + sx) u_1]_x = -[\delta F / (1 - \delta)] (\eta u_1)_x, \tag{2.22}$$

$$(1 - \delta)\left(\partial_t + F \partial_x - R_E^{-1} \partial_{xx}\right) u_2 + c_D(2 u_2 / F - \eta) + (\eta + \delta p_1)_x$$
$$= F(1 - \delta)(\eta_x / R_E - u_2)\partial_x u_2 - c_D(u_2 - \delta \eta)^2 / F + \text{h.o.t.}, \tag{2.23}$$

$$(\partial_t + F \partial_x)\eta + \partial_x u_2 = -F (\eta u_2)_x, \tag{2.24}$$

$$(1 - \delta) p_2 = \eta + \delta p_1, \tag{2.25}$$

where the bottom friction term in (2.11) has been Taylor expanded and cubic and higher order nonlinearities have been neglected (h.o.t. means higher order terms).

The linear stability problem, obtained by neglecting all the quadratic nonlinear terms in (2.21) through to (2.24) can be written in the form, after a little algebra,

$$\mathcal{L}\left[(1 + sx) u_1\right] + \delta \left(\partial_t - R_E^{-1} \partial_{xx}\right) \partial_t u_1 = 0, \tag{2.26}$$

with the auxiliary relations

$$\partial_x p_1 = -\left(\partial_t - R_E^{-1} \partial_{xx}\right) u_1, \tag{2.27}$$

$$\eta_t = [(1 + sx) u_1]_x, \qquad (2.28)$$

$$\partial_t u_2 = -(\partial_t + F\partial_x) [(1 + sx) u_1] \qquad (2.29)$$

(p_2 can be determined from (2.25)), where $\mathscr{L}$ is the linear constant coefficient partial differential operator

$$\mathscr{L} \equiv (1 - \delta) \left(\partial_t + F\partial_x - R_E^{-1}\partial_{xx}\right) (\partial_t + F\partial_x) - \partial_{xx} + c_D\partial_x + (2c_D/F) (\partial_t + F\partial_x). \qquad (2.30)$$

3. Stability characteristics in the small slope approximation

The small slope approximation is to neglect the sx term in (2.26) alone. Physically, within the context of the linear stability equation (2.26) this approximation is equivalent to removing the mean depth variations in the upper layer alone, associated with the sloping bottom. It is important to appreciate that neglecting this term is not the same as making a flat bottom assumption. The effect of a sloping bottom is still retained in the abyssal current momentum equations. Given that $s_*/(H - h_*) \simeq O(4 \times 10^{-5}\,m^{-1})$ (see (2.14) and (2.15)), from the viewpoint of normal mode perturbation stability theory, the role of the sx term in (2.26) is to induce slowly varying geometrical optics corrections to the phase and amplitude. These corrections will be described in §4. Moreover, in §4 the exact solution to (2.26) with $s > 0$ is obtained in the $R_E \to \infty$ limit, and its asymptotic relation to the solutions described in this section is further described. From the mathematical perspective, however, the distinct advantage in neglecting this term is that the linear stability equations correspond to a well-posed Cauchy problem for $x \in \mathbb{R}$, which permits temporally amplifying, spatially periodic normal modes (without having to satisfy appropriate regularity conditions at the point of zero mean depth for the upper layer in which $1 + sx = 0$). Indeed, from the perspective of modelling the dynamics of abyssal overflows within the ocean, it is reasonable to assume that the mean thickness of the overlying water column is never close to zero, and thus, since $0 < s < 1$ and $x \simeq O(1)$, it is not completely unreasonable to approximate $1 + sx \approx 1$ in (2.26).

If one assumes $s = 0$ in (2.26), it follows

$$\left[\mathscr{L} + \delta \left(\partial_t - R_E^{-1}\partial_{xx}\right) \partial_t\right] u_1 = 0, \qquad (3.1)$$

which has the normal mode solution

$$u_1 = A \exp(ikx + \sigma t) + \text{c.c.}, \qquad (3.2)$$

where c.c. means the complex conjugate of the preceding term; k is the real-valued downslope wavenumber; and σ is the complex-valued 'growth rate', provided the dispersion relation

$$\sigma = \sigma_\pm \equiv -\mathrm{i}(1 - \delta) Fk - \left(\frac{c_D}{F} + \frac{k^2}{2R_E}\right)$$
$$\pm \sqrt{\left(\frac{c_D}{F} + \frac{k^2}{2R_E}\right)^2 + \left[\delta (1 - \delta) F^2 - 1\right] k^2 - \mathrm{i}c_D k (1 + 2\delta)}, \qquad (3.3)$$

holds, where the branch cut is taken along the negative real axis. This dispersion relation is similar but not identical to that derived in Swaters (2006a). The differences are that (3.3) has the relatively fast barotropic mode removed; the coefficients in (3.3) look quite different, but that is because of the different non-dimensional scheme used, and most importantly, the dispersion relation derived here, unlike that in Swaters

(2006*a*), is valid in the limit $c_D \to 0$ or $s \to 0$. That is (3.3) is valid for a substantially more complete range of destabilizations from purely inertial–inviscid KH instability to the non-stratified frictionally induced instability of abyssal downslope flow. Due to the underlying linearity of the stability problem, the $\delta = 0$ limit of (3.3) is the dispersion relation for the equivalent-barotropic problem (irrespective of the fact the dependent variable is u_1 in (3.1)). In this situation only frictional destabilization occurs, since there is no KH instability possible in a reduced-gravity shallow-water model.

There is one last useful observation about (3.3) that is appropriate to make. In the $R_E \to \infty$ limit, (3.3) can be written as a complex-valued polynomial equation that is quadratic with respect to both σ and k, individually. Thus, while it is obviously clear from (3.3) that *given k*, there are *two* complex-valued growth rates that are solutions (σ_+ and σ_- are not necessarily c.c.s of each other), (3.3) can be turned around to imply that *given σ* there *two* possibly complex-valued 'wavenumbers' k that are solutions. This point will become important in §4, when an exact solution to (2.26) is presented for the $R_E \to \infty$ limit and its relationship to (3.1)–(3.3) is described.

3.1. *Marginal stability boundary, special limits and a high-wavenumber cutoff*

It follows from (3.3) that stability occurs for a given mode when $\mathrm{Re}\,(\sigma_+) \leqslant 0$, i.e.

$$\mathrm{Re}\left\{ \sqrt{\left(\frac{c_D}{F} + \frac{k^2}{2R_E}\right)^2 + \left[\delta\,(1-\delta)\,F^2 - 1\right]k^2 - \mathrm{i}c_D k\,(1+2\delta)} \right\} \leqslant \frac{c_D}{F} + \frac{k^2}{2R_E}. \quad (3.4)$$

If one introduces the Euler representation (that serves to define the real numbers α and β)

$$\alpha \exp\,(\mathrm{i}\beta) = \left(\frac{c_D}{F} + \frac{k^2}{2R_E}\right)^2 + \left[\delta\,(1-\delta)\,F^2 - 1\right]k^2 - \mathrm{i}c_D k\,(1+2\delta),$$

(3.4) takes the form

$$\sqrt{\alpha}\cos\,(\beta/2) \leqslant \frac{c_D}{F} + \frac{k^2}{2R_E} \implies \alpha\,[1+\cos\,(\beta)] \leqslant 2\left(\frac{c_D}{F} + \frac{k^2}{2R_E}\right)^2,$$

on account of the location of the branch cut. If α and β are substituted in (3.4), it can be written as

$$\sqrt{\left[\left(\frac{c_D}{F} + \frac{k^2}{2R_E}\right)^2 + \left[\delta\,(1-\delta)\,F^2 - 1\right]k^2\right]^2 + [c_D k\,(1+2\delta)]^2}$$

$$\leqslant \left(\frac{c_D}{F} + \frac{k^2}{2R_E}\right)^2 - \left[\delta\,(1-\delta)\,F^2 - 1\right]k^2. \quad (3.5)$$

Clearly, the right-hand side of (3.5) must be positive for the inequality to hold. Thus, a *necessary* condition for stability is

$$[\delta(1-\delta)F^2 - 1]k^2 \leqslant \left(\frac{c_D}{F} + \frac{k^2}{2R_E}\right)^2. \quad (3.6)$$

Conversely, a *sufficient* condition for instability is the inequality in (3.6) be (strictly) reversed. Qualitatively, this demonstrates the destabilizing effect of increasing F (the shear) and the stabilizing effect of horizontal friction (realized through decreasing

R_E). In a moment, much sharper stability conditions will be established that will supersede (3.6), but for now (3.6) is assumed to hold.

If (3.6) holds, then both sides of (3.5) can be squared to yield

$$k^2 \left(\frac{c_D}{F} + \frac{k^2}{2R_E} \right)^2 [1 - \delta(1-\delta)F^2] \geqslant [c_D k (1 + 2\delta)/2]^2. \tag{3.7}$$

From (3.7) it follows the $k = 0$ mode is unconditionally stable. If $k \neq 0$, then the stability condition (3.7) reduces to

$$\left(\frac{c_D}{F} + \frac{k^2}{2R_E} \right)^2 [1 - \delta(1-\delta)F^2] \geqslant [c_D(1+2\delta)/2]^2. \tag{3.8}$$

Again, for (3.8) to hold it is *necessary*

$$\delta(1-\delta)F^2 \leqslant 1, \tag{3.9}$$

or else the left-hand side of (3.8) is negative, while the right-hand side is positive. Note if (3.9) holds, (3.6) is automatically satisfied, and thus (3.9) is the stronger constraint. In §3.1.6 a bulk Richardson number interpretation is given for (3.9).

Based on the properties of monotonic continuous functions (as argued below), it immediately follows there exists a unique F_B in the interval $0 < F_B < 1/\sqrt{\delta(1-\delta)}$, satisfying

$$(\nu + 1/F_B)^2 [1 - \delta(1-\delta)F_B^2] = [(1+2\delta)/2]^2, \tag{3.10}$$

where

$$\nu \equiv k^2/(2c_D R_E) \geqslant 0$$

((3.10) is just (3.8) with an equality). Consequently, it follows for a given mode

$$0 \leqslant F \leqslant F_B \iff \text{stability (i.e. } F > F_B \iff \text{instability)}, \tag{3.11}$$

and hence the stability boundary, denoted as F_B, for a fixed wavenumber k, will be given by

$$F = F_B(\nu, \delta). \tag{3.12}$$

Consider (3.10) for fixed $\nu \geqslant 0$ and $\delta \in (0, 1)$. It follows that the right-hand side of (3.10) is a fixed positive real number, and the left-hand side of (3.10) is a continuous function with respect to F_B for all $F_B > 0$ with the properties $\lim_{F_B \to 0^+}$ of the left-hand side of (3.10) $= \infty$, the left-hand side of (3.10) $= 0$ for $F_B = 1/\sqrt{\delta(1-\delta)}$ and the left-hand side of (3.10) is a monotonic decreasing continuous function as F_B increases in the interval $F_B \in (0, 1/\sqrt{\delta(1-\delta)})$. Consequently, there exists a *unique* $F_B(\nu, \delta)$ in the interval $0 < F_B < 1/\sqrt{\delta(1-\delta)}$, satisfying (3.10).

Equation (3.10) can be rearranged into the quartic

$$4\nu^2 \delta(1-\delta)F_B^4 + 8\nu\delta(1-\delta)F_B^3 + (1 + 8\delta - 4\nu^2)F_B^2 - 8\nu F_B = 4, \tag{3.13}$$

for which it is possible to find an explicit positive solution if it exists. Unfortunately, this representation is not particularly illuminating and is therefore not given here. A number of important special limits for F_B can be easily determined (e.g. $\delta = 0$, $\delta = 1$, $\nu = 0$ and $\nu \to \infty$) and some of these reduce to well-known results. These are described below. Figure 2 shows a contour plot of F_B in the (ν, δ) plane for $0 \leqslant \nu \leqslant 2$ and $0 < \delta < 1$ for selected contour values. Apart from near the $\delta = 0$ and $\delta = 1$ boundaries (of which more will be said later), figure 2 shows F_B does not vary dramatically and has a characteristic value of about $F_B \simeq 2$.
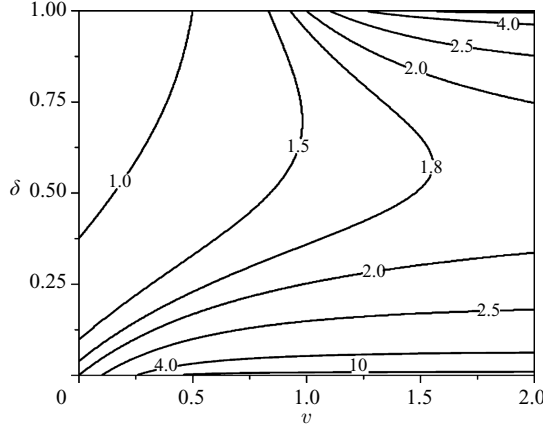
FIGURE 2. Contour plot of the stability boundary F_B in the (ν, δ)-plane for selected contours. Instability occurs for $F > F_B$. Dimensionally, $F_B = 1$ corresponds to a downslope abyssal flow speed of about 37 cm s^{-1}.

3.1.1. *The $R_E \to \infty$ limit*

The $R_E \to \infty$ ($\nu = 0$) limit of (3.10) or (3.13) reduces to a quadratic equation for F_B, the positive solution of which is given by

$$F_B|_{\nu=0} = 2/\sqrt{1 + 8\delta}. \tag{3.14}$$

Equation (3.14) determines the value of F_B along the δ-axis in figure 2. Thus, in the large-R_E limit, the presence of an upper layer acts to destabilize the flow, since F_B decreases as δ increases. In summary, for $R_E \to \infty$, the flow is stable for $0 \leqslant F \leqslant 2/\sqrt{1 + 8\delta}$ and unstable for $F > 2/\sqrt{1 + 8\delta}$.

In §3.2, it will be shown the growth rate of the unstable modes in the $R_E \to \infty$ limit is bounded for all wavenumbers when $2/\sqrt{1 + 8\delta} < F \leqslant 1/\sqrt{\delta(1 - \delta)}$ but exhibits an ultraviolet catastrophe if $F > 1/\sqrt{\delta(1 - \delta)}$ – i.e. the most unstable mode has an infinite growth rate and occurs for a infinite wavenumber. Mathematically, the ultraviolet catastrophe is a consequence of the fact that the linear stability problem (3.1), if $R_E \to \infty$, becomes elliptic for $F > 1/\sqrt{\delta(1 - \delta)}$, for which the Cauchy problem is ill posed. If $R_E < \infty$, the ultraviolet catastrophe does not occur, but the most unstable mode, with bounded growth rate, nevertheless occurs for $|k| \to \infty$. Again, this is shown in §3.2.

3.1.2. *The marginal stability boundary*

The infinite R_E stability boundary (3.14) provides a sharp lower bound for $|F_B(\nu, \delta)|$ $\forall\ \nu \geqslant 0$ from which the *marginal* stability boundary can be derived. Observe that it follows from (3.10)

$$\left[1 - \delta(1 - \delta) F_B^2\right] \leqslant \left[F_B(1 + 2\delta)/2\right]^2 \implies F_B^2 \geqslant 4/(1 + 8\delta).$$

Thus, it is possible to conclude

$$\frac{2}{\sqrt{1 + 8\delta}} = F_B|_{\nu=0} \leqslant |F_B(\nu, \delta)| \leqslant \frac{1}{\sqrt{\delta(1 - \delta)}} \forall\ \nu \geqslant 0. \tag{3.15}$$

Consequently, the *marginal stability boundary*, denoted as F_m, is given by
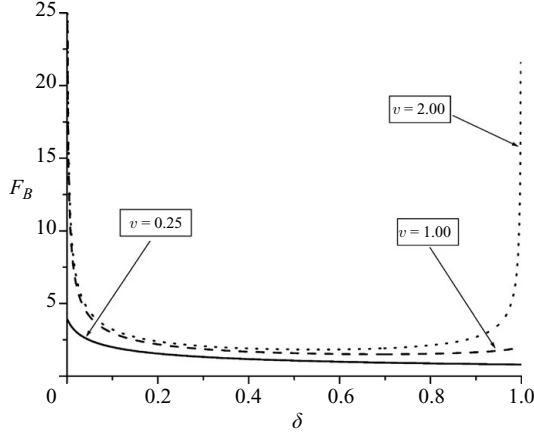
$$F_m \equiv 2/\sqrt{1 + 8\delta}. \tag{3.16}$$

FIGURE 3. Graphs of the stability boundary F_B versus δ for $\nu = 0.25$, 1.0 and 2.0, respectively.

That is if $F > F_m$, there will exist a non-empty interval of wavenumbers that are unstable, i.e. for which $\mathrm{Re}\,(\sigma_+) > 0$.

3.1.3. The $\delta = 0$ and $\delta \to 1$ limits

The $\delta = 0$ limit (corresponding to the ν-axis in figure 2) is the equivalent-barotropic or reduced-gravity situation in which the overlying layer is infinitely deep and in a hydrostatic rest state (i.e. contains no dynamics). Within the context of the *reduced-gravity* shallow-water equations, it is well known KH instability is not possible, and thus, for the problem examined here, only frictional destabilization is possible. Thus, in the $\delta = 0$ limit, F_B must reduce to the classical result associated with roll-wave instability (see, e.g., Jeffreys 1925; Whitham 1974; Baines 1995; Balmforth & Mandre 2004). The $\delta = 0$ limit of (3.10) or (3.13) reduces to a quadratic equation for F_B, the positive solution of which, if it exists, is given by

$$\frac{1}{F_B|_{\delta=0}} + \nu \equiv \frac{1}{F_B|_{\delta=0}} + \frac{k^2}{2c_D R_E} = \frac{1}{2}. \tag{3.17}$$

In the infinite-Reynolds-number limit, (3.17) reduces to the classical roll-wave result $F_B = 2$; i.e. bottom-friction-induced instability occurs only when the Froude number satisfies $F > 2$, and the flow is stable if $0 < F \leqslant 2$. However, if $\nu > 0$, then (3.17) implies

$$F_B|_{\delta=0} = \begin{cases} 2/(1 - 2\nu) & \text{if } 0 \leqslant \nu < 1/2, \\ \infty & \text{if } \nu \geqslant 1/2. \end{cases} \tag{3.18}$$

Thus, along the ν-axis in figure 2, $F_B|_{\delta=0}$ increases as ν increases and becomes unbounded as $\nu \to 1/2$ and remains so thereafter. Since F_B depends continuously on δ and ν, it follows for δ slightly larger than zero F_B will be bounded for $0 \leqslant \nu < 1/2$ but will become large as ν passes through $1/2$. This is the reason for the increase in F_B along the ν-axis in figure 2 as ν increases past $1/2$. This structure is further illustrated in figure 3 which shows graphs of F_B versus δ for $\nu = 0.25$, 1.0 and 2.0, respectively. The $F_B|_{\nu=0.25}$ curve is bounded for $\delta = 0$ (with value 4.0) and monotonically decreases as δ increases until it reaches the value $F_B|_{\nu=0.25} = 0.8$ (see (3.19)) for $\delta = 1$. On the other hand, the $F_B|_{\nu=1}$ curve is unbounded for $\delta = 0$ and decreases with increasing δ until near the $\delta = 1$ boundary at which it slightly increases to the value $F_B|_{\nu=1} = 2.0$ (see (3.19)).

A similar behaviour happens for $\delta = 1$. But an important comment must be made first. Even though a solution formally exists for F_B if $\delta = 1$ (see (3.10) or (3.11)) this solution is unphysical for the approximations made here. The assumption $\delta = 1 \Longleftrightarrow h_* = H$ implies $s \to \infty$ (see (2.14)), so it is not possible to rationally neglect the 'sx' term in (2.26) as has been done in this section. Moreover, additional problems develop in this limit, since the explicitly baroclinic scalings introduced in (2.6)–(2.8) implicitly assume $0 < h_* < H$. Nevertheless, the $F_B|_{\delta=1}$ solution is important in understanding the qualitative properties of F_B, where δ is close to but still less than 1.0 which is, formally at least, allowed.

In the limit $\delta \to 1$, (3.10) or (3.13) reduces to a quadratic equation for F_B, the positive solution of which, if it exists, is given by

$$\frac{1}{F_B|_{\delta=1}} + \nu = \frac{3}{2}, \tag{3.19}$$

which implies

$$F_B|_{\delta=1} = \begin{cases} 2/(3-2\nu) & \text{if } 0 \leqslant \nu < 3/2, \\ \infty & \text{if } \nu \geqslant 3/2. \end{cases} \tag{3.20}$$

Thus, along the $\delta = 1$ line in figure 2, $F_B|_{\delta=1}$ increases as ν increases and becomes unbounded as $\nu \to 3/2$ and remains so thereafter. This structure is shown in figure 3 for the $F_B|_{\nu=2}$ curve. The $F_B|_{\nu=2}$ curve is unbounded as $\delta \to 0^+$ *or* $\delta \to 1^-$. Thus, $F_B|_{\nu=2}$ decreases as δ increases, reaching its minimum value of about 1.83 at $\delta \approx 0.55$ after which it increases, eventually becoming unbounded as $\delta \to 1^-$. Finally, the $F_B|_{\nu=2}$ curve in figure 2 also illustrates the generic property for $\nu > 2$ that $F_B \approx 2$ except when δ is close to 0 or 1.

3.1.4. *The $c_D = 0$ limit*

In the $c_D = 0$ ($\nu \to \infty$) limit, there can be no frictionally induced instability, and only KH destabilization is possible. With respect to determining the stability boundary F_B, the $c_D = 0$ limit is equivalent to the zero-Reynolds-number ($R_E \to 0$) limit or the high-wavenumber limit, $|k| \to \infty$. The $c_D = 0$ limit of (3.10) or (3.13) reduces to a quadratic equation for F_B, the positive solution of which is given by

$$F_B|_{c_D=0} = 1/\sqrt{\delta(1-\delta)}. \tag{3.21}$$

The graph given by (3.21) will possess vertical asymptotes at $\delta = 0$ and $\delta = 1$, respectively, has a 'parabolic shape' with positive concavity and is symmetric about $\delta = 1/2$ (where its minimum is located at $\delta = 1/2$ with value 2; see figure 6a).

Figure 4 shows a graph of $F_B|_{\delta=3/8}$ versus ν for $\delta = 3/8$ (characteristic of the DSO; see (2.15)). One can see the rapid increase of $F_B|_{\delta=3/8}$ from its value at $\nu = 0$ ($F_B|_{\delta=3/8}(\nu = 0) = 1$; see (3.14)) and its asymptotic approach to the value determined by (3.21), i.e. $F_B|_{\delta=3/8}(\nu \to \infty) \simeq 2.07$. It is now shown (3.21) determines the boundary between the parameter regions in which a high wavenumber possibly exists and in which it does not exist.

3.1.5. *High-wavenumber cutoff*

If $F \geqslant 1/\sqrt{\delta(1-\delta)}$, (3.8) can never be satisfied for any choice of k, since its left-hand side $\leqslant 0$ for all k and since its right-hand side $\geqslant 0$ (unless, trivially, both sides are zero). However, for the sub-interval of unstable Froude numbers given by $F_B < F < 1/\sqrt{\delta(1-\delta)}$, (3.8) *will* be satisfied for those wavenumbers for which
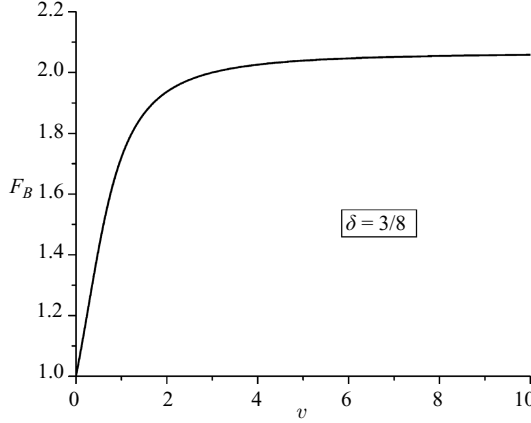
FIGURE 4. Graph of F_B versus ν for $\delta = 3/8$.

$|k| \geqslant k_{cutoff}$, where

$$\left(\frac{1}{F} + \frac{k^2_{cutoff}}{2c_D R_E} \right)^2 \left[1 - \delta \left(1 - \delta \right) F^2 \right] = \left[\left(1 + 2\delta \right) / 2 \right]^2 ,$$

which can be rearranged into

$$k_{cut-off} \equiv \sqrt{ \frac{c_D R_E \left[\left(1 + 8\delta \right) F^2 - 4 \right]}{F \sqrt{1 - \delta \left(1 - \delta \right) F^2} \left[\left(1 + 2\delta \right) F + 2\sqrt{1 - \delta \left(1 - \delta \right) F^2} \right]} } . \tag{3.22}$$

On account of (3.15), $(1 + 8\delta)F^2 \geqslant 4$ if $F \geqslant F_B$, so the numerator within the outermost square root in (3.22) is non-negative.

It follows from (3.22)

$$\lim_{F \,\downarrow 2/\sqrt{1 + 8\delta}} k_{cutoff} = 0, \tag{3.23}$$

$$\lim_{F \,\uparrow 1/\sqrt{\delta(1 - \delta)}} k_{cutoff} = \infty. \tag{3.24}$$

The high-wavenumber cutoff limit given by (3.23) is simply a consequence of the fact $F = 2/\sqrt{1 + 8\delta}$ is the marginal stability boundary, and thus it follows from (3.14) all wavenumbers satisfy (3.8). The high-wavenumber cutoff limit given by (3.24) is simply a consequence of the fact that if $F = 1/\sqrt{\delta(1 - \delta)}$, there are no wavenumbers that can satisfy (3.8).

Figure 5(a) shows graphs of k_{cutoff} versus F over the domain $2/\sqrt{1 + 8\delta} \leqslant F < 1/\sqrt{\delta(1 - \delta)}$ for $\delta = 0.1$, 3/8 and 0.8 (meant to be indicative of a 'thin', 'DSO-like' and a 'thick' abyssal overflow), respectively, for *fixed* $c_D = 1.0$ and $R_E = 225.0$. For a given value of δ, figure 5(a) shows the 'gradual increase in k_{cutoff} as F increases past the point of marginal stability given by $2/\sqrt{1 + 8\delta}$, becoming 'rapidly' unbounded as $F \to 1/\sqrt{\delta(1 - \delta)}$. Based on figure 5(a), one can roughly estimate $k_{cutoff} \approx 10$ for intermediate values of the Froude numbers that are removed from the end points $2/\sqrt{1 + 8\delta}$ or $1/\sqrt{\delta(1 - \delta)}$. In summary, for $F_B < F < 1/\sqrt{\delta(1 - \delta)}$, a high-wavenumber cutoff exists (again, assuming $R_E < \infty$) and is given by $|k| = k_{cutoff}$ with instability occurring for those wavenumbers that satisfy $|k| \in (0, k_{cutoff})$. If $F \geqslant 1/\sqrt{\delta(1 - \delta)}$, there is no high-wavenumber cutoff (i.e. $k_{cutoff} = \infty$, irrespective of whether $R_E < \infty$ or not), and there is instability for all non-zero wavenumbers.
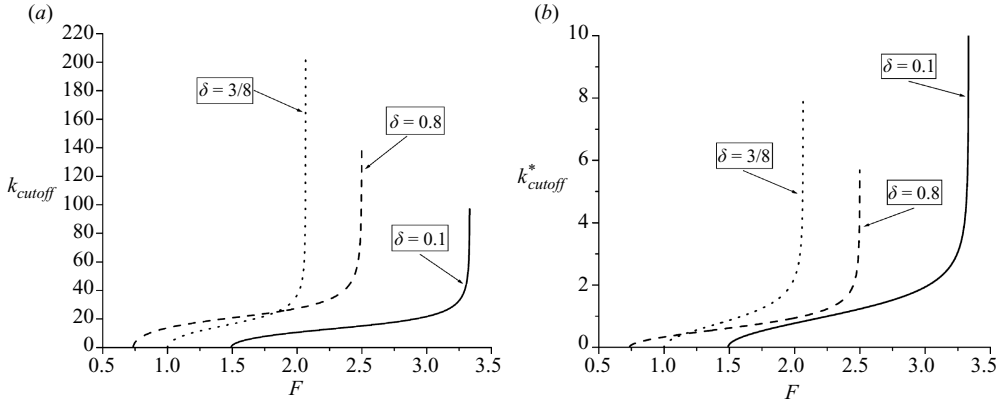
FIGURE 5. (*a*) Graphs of the high-wavenumber cutoff k_{cutoff} versus F for $\delta = 0.1$, 3/8 and 0.8, respectively, with $c_D = 1.0$ and $R_E = 225.0$. Dimensionally, $F = 1$ corresponds to a downslope abyssal flow speed of about 37 cm s^{-1}. (*b*) Graphs of the dimensional high-wavenumber cutoff k^*_{cutoff} versus F for $\delta = 0.1$, 3/8 and 0.8, respectively, with $l_D = 1225$ m. The units for k^*_{cutoff} are km^{-1}.

It is of interest to determine the *dimensional* high-wavenumber cutoff, denoted by k^*_{cutoff}. If the definitions for c_D and R_E from (2.14) are substituted into (3.22), it follows

$$k^*_{cutoff} = \frac{1}{l_D}\sqrt{\frac{(1-\delta)\left[(1+8\delta)F^2 - 4\right]}{\sqrt{1-\delta(1-\delta)F^2}[(1+2\delta)F + 2\sqrt{1-\delta(1-\delta)F^2}]}}, \qquad (3.25)$$

where l_D is the 'dissipation' length scale described in §2. Figure 5(*b*) shows graphs of k^*_{cutoff} versus F over the domain $2/\sqrt{1+8\delta} \leqslant F < 1/\sqrt{\delta(1-\delta)}$ for $\delta = 0.1$, 3/8 and 0.8, respectively, for $l_D = 1225$ m. Figure 5(*b*) does not correspond to figure 5(*a*) divided by the length scale L because $c_D R_E = (1-\delta)F(L/l_D)^2$ (see (2.14)) and thus varies with δ. For intermediate values of F, figure 5(*b*) suggests $k^*_{cutoff} \approx 1$ km^{-1}, which corresponds to a cutoff wavelength about 6.3 km. That is, it is to be expected the most unstable modes will have typical wavelengths longer than 6.3 km. In turn, this suggests the topographic length scale $l_s \simeq 15$ km described in §2 is not an inappropriate choice for a dynamical length scale.

It is important to appreciate the limitations of the KH instability examined here. Since the governing equations are based on a two-layer shallow-water model, the KH instability examined here is hydrostatic, and moreover, the only unstable flow configuration that can be considered corresponds to a vortex sheet with a mean velocity discontinuity across the interface between the abyssal and upper layers. In both the two-layer shallow-water equations and the non-hydrostatic equations, in the inviscid limit, it is well known (see, e.g., LeBlond & Mysak 1978; Drazin & Reid 1981) that an ultraviolet catastrophe occurs in the linear stability analysis for the vortex sheet. However, in the non-hydrostatic model, the shear layer KH instability (i.e. the mean velocity is continuous but may possess discontinuities in the mean vorticity) has the most unstable mode located at a finite wavenumber and has a high-wavenumber cutoff. The shear layer KH instability cannot be examined with the shallow-water equations and thus lies outside the applicability of the model considered here. This is a shortcoming of the present analysis and a potentially physically important problem for abyssal overflows that warrants further investigation.
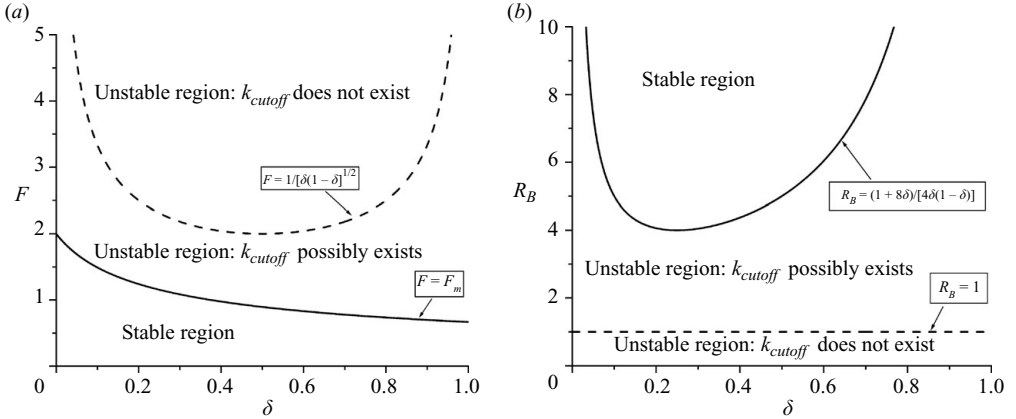
FIGURE 6. (a) Stability diagram in the (δ, F)-plane, where F is the Froude number and δ is the ratio of the thickness of the abyssal current to the overall thickness of the water column. The solid curve $F = F_m(\delta)$ (see (3.16)) is the marginal stability boundary, and the point of marginal stability is located at $F = F_m(1) = 2/3$. The dashed curve $F = 1/\sqrt{\delta(1-\delta)}$ is the boundary within the unstable region separating the sub-regions in which a high-wavenumber cutoff k_{cutoff} exists (only if $R_E < \infty$) and in which k_{cutoff} does not exist. If $R_E \to \infty$, the growth rates are bounded for all $k \geqslant 0$ in the region $F_m < F \leqslant 1/\sqrt{\delta(1-\delta)}$, and an ultraviolet catastrophe occurs in the region $F > 1/\sqrt{\delta(1-\delta)}$. Dimensionally, $F = 1$ corresponds to a downslope abyssal flow speed of about 37 cm s^{-1}. (b) Stability diagram in the (δ, R_B)-plane, where R_B is the bulk Richardson number (3.25). The solid curve $R_B = R_{B_m}(\delta)$ (see (3.26)) is the marginal stability boundary. The dashed $R_B = 1$ line is the boundary within the unstable region separating the sub-regions in which a high-wavenumber cutoff exists (if $R_E < \infty$) and in which it does not exist. If $R_E \to \infty$, the growth rates associated with the unstable modes are bounded for all $k \geqslant 0$ in the region $1 \leqslant R_B < R_{B_m}$, and an ultraviolet catastrophe occurs in the region $R_B < 1$.

3.1.6. Stability diagrams

The results of this section can be summarized in two equivalent stability diagrams. Figure 6(a) shows the stability diagram in the (δ, F)-plane. This is the representation most typically used when describing the stability characteristics associated with frictional destabilization, e.g. roll-wave formation. The solid curve in figure 6(a) given by $F = F_m$ is the marginal stability boundary (3.16). Instability occurs in the region $F > F_m$, and the flow is stable in the region $F \leqslant F_m$. Figure 6(a) illustrates the destabilizing influence of an upper layer with finite thickness; i.e. the minimum Froude number required for instability decreases as δ increases for $\delta \in (0, 1)$.

The dashed curve $F = 1/\sqrt{\delta(1-\delta)}$ is the boundary within the unstable region that separates the sub-region (i.e. $F_m < F < 1/\sqrt{\delta(1-\delta)}$) in which a high-wavenumber cutoff exists (if $R_E < \infty$) and the sub-region in which it does not exist (i.e. $F \geqslant 1/\sqrt{\delta(1-\delta)}$). It will be shown in §3.2 that if $R_E < \infty$, the growth rates are bounded $\forall\, k \geqslant 0$ throughout the region $F_m < F$. On the other hand, it will be shown in §3.2 that in the $R_E \to \infty$ limit, the growth rates are bounded $\forall\, k \geqslant 0$ only in the sub-region $F_m < F \leqslant 1/\sqrt{\delta(1-\delta)}$, but an ultraviolet catastrophe occurs in the sub-region $F > 1/\sqrt{\delta(1-\delta)}$. Finally, it is noted the minimum of the curve $F = 1/\sqrt{\delta(1-\delta)}$ occurs for $\delta = 1/2$ with value $F = 2$, and the graph $F = 1/\sqrt{\delta(1-\delta)}$ always lies above $F = F_m$. The point of marginal stability is given by the minimum of F_m, i.e. $F = F_m|_{\delta=1} = 2/3$. Specifically, with respect to the DSO, where it has been estimated $\delta \simeq 3/8$ and $F \simeq 2.7$, figure 6(a) suggests the DSO is susceptible to the instability described here, and moreover, the transition may occur very near the

boundary (see figure 5) in which there is no high-wavenumber cutoff. This in turn suggests the potential need to examine the transition process using a non-hydrostatic theory.

From the viewpoint of how KH instability is typically described, it is useful to recast the stability diagram in terms of the bulk (i.e. vertically averaged over the entire water column) Richardson number, denoted by R_B and given by

$$R_B \equiv \frac{g'H}{U^2} = \frac{1}{\delta(1-\delta)F^2}, \tag{3.26}$$

where (2.8) has been used. In terms of R_B, the marginal stability boundary (3.16) and the $F = 1/\sqrt{\delta(1-\delta)}$ stability boundary are given by, respectively,

$$F = F_m \equiv 2/\sqrt{1+8\delta} \Longleftrightarrow R_B = R_{B_m} \equiv \frac{1+8\delta}{4\delta(1-\delta)}, \tag{3.27}$$

$$F = 1/\sqrt{\delta(1-\delta)} \Longleftrightarrow R_B = 1, \tag{3.28}$$

where it is understood attention is restricted to downslope flows. Figure 6(*b*) shows the stability diagram in the (δ, R_B)-plane. The solid curve in figure 6(*b*) is the marginal stability boundary given by (3.27). Instability occurs in the region $R_B < R_{B_m}$ with stability in the region $R_B \geqslant R_{B_m}$.

The dashed line $R_B = 1$ in figure 6(*b*) is the boundary within the unstable region separating the sub-region in which a high-wavenumber cutoff exists (i.e. $1 < R_B < R_{B_m}$ if $R_E < \infty$) and in which it does not exist (i.e. $R_B < 1$). Following the discussion given above for figure 6(*a*), if $R_E < \infty$, the growth rates are bounded $\forall\ k \geqslant 0$ throughout the region $R_B < R_{B_m}$. On the other hand, in the $R_E \to \infty$ limit, the growth rates are bounded $\forall\ k \geqslant 0$ only in the sub-region $1 \leqslant R_B < R_{B_m}$ with an ultraviolet catastrophe developing in the sub-region $R_B < 1$. Finally, again, it is noted the minimum of the curve $R_B = R_{B_m}$ occurs for $\delta = 1/4$ with value $R_B = 4$, and the graph $R_B = R_{B_m}$ always lies above $R_B = 1$. The minimum of the curve $R_B = R_{B_m}$ is *not* the point of marginal stability, and indeed, there is no finite point of marginal stability in terms of the bulk Richardson number. This underscores the utility of characterizing the stability properties in terms of the Froude number for the two-layer shallow-water model examined here.

3.2. *Growth rate, frequency and wavelength characteristics of the unstable modes*

Since $\mathrm{Re}(\sigma_-) \leqslant \mathrm{Re}(\sigma_+)$, the stability of the flow is solely determined by the σ_+ root of the dispersion relation (3.3). Figure 7(*a*) is a contour plot of $\mathrm{Re}(\sigma_+)$ in the (k, F)-plane for $\delta = 3/8$, $c_D = 1.0$ and $R_E = 225.0$ for selected contours. The solid contours correspond to positive $\mathrm{Re}(\sigma_+)$, i.e. the unstable modes. The dashed contours correspond to where the σ_+ mode exponentially decays with respect to t (and thus the flow is asymptotically stable).

The 0-contour, where $\mathrm{Re}(\sigma_+) = 0$, corresponds to the high-wavenumber cutoff curve $k = k_{cutoff}$ as determined by (3.22) or, equivalently, the stability boundary $F = F_B(\nu, \delta)$ as determined by (3.10). For $F > 1/\sqrt{\delta(1-\delta)}|_{\delta = 3/8} \simeq 2.07$, $k_{cutoff} = \infty$, and there is instability for all $k > 0$. In the lower left-hand corner of figure 7(*a*) the 0-contour appears to be smoothly approaching the F-axis but then abruptly turns to approach the k-axis. This is a consequence of the contouring software trying to adapt to the singular structure of the stability boundary near $k = 0$. It follows directly from (3.3) $\mathrm{Re}(\sigma_+) = 0$ for $k = 0$ (see, also, the discussion following (3.7)). However, if $k > 0$ (no matter how small), then instability only occurs if $F > F_m|_{\delta = 3/8} = 1$ (see (3.16)).
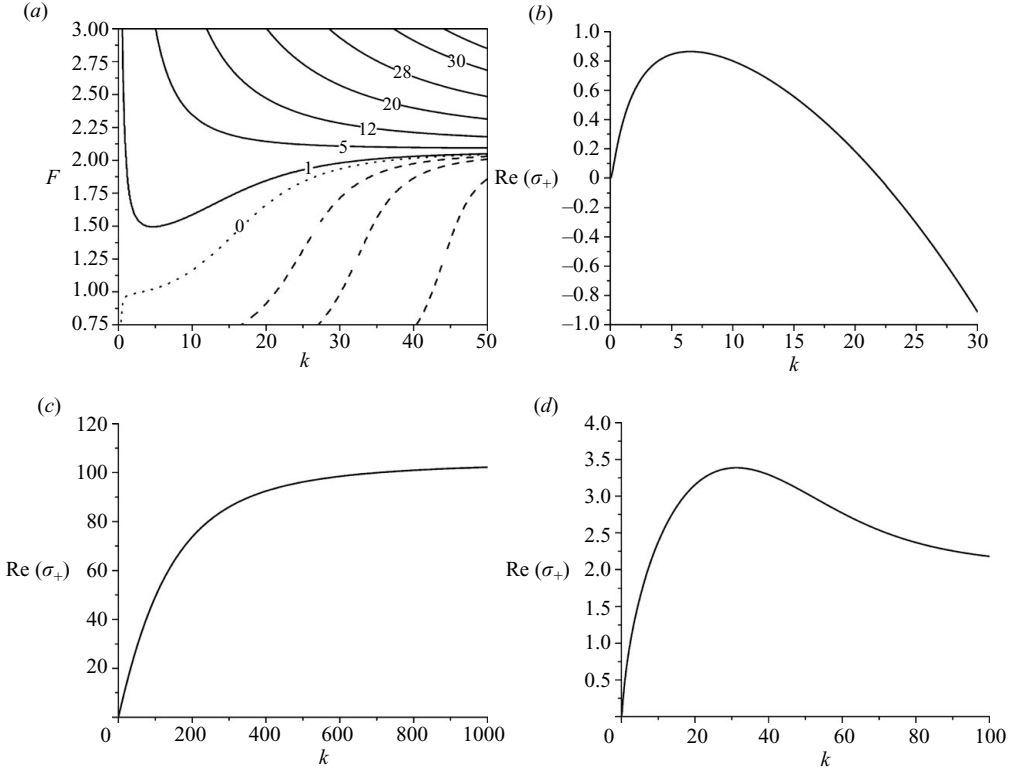
FIGURE 7. (a) Contour plot of $\mathrm{Re}\,(\sigma_+)$ in the (k, F)-plane as determined by (3.3) for $\delta = 3/8$, $c_D = 1.0$ and $R_E = 225.0$ for selected contours. The solid contours correspond to the growth rates of the unstable modes with positive $\mathrm{Re}\,(\sigma_+)$. The dashed contours correspond to where the σ_+ mode exponentially decays with respect to t. (The flow is asymptotically stable.) The 0-contour, where $\mathrm{Re}\,(\sigma_+) = 0$, corresponds to the high-wavenumber cutoff $k = k_{cutoff}$. For $F > 1/\sqrt{\delta(1-\delta)}|_{\delta=3/8} \simeq 2.07$, $k_{cutoff} = \infty$, and there is instability for all $k > 0$. Dimensionally, $\mathrm{Re}\,(\sigma_+) = 1$ (-1) corresponds to an e-folding amplification (decay) time of about 11 hours; $F = 1$ corresponds to a downslope abyssal flow speed of about 37 cm s^{-1}; and $k = 10$ corresponds to a wavelength of about 9.4 km. (b) Graph of $\mathrm{Re}\,(\sigma_+)$ versus k along the section $F = 1.75$ in (a). Since $F < 1/\sqrt{\delta(1-\delta)}|_{\delta=3/8} \simeq 2.07$ and $R_E < \infty$, a high-wavenumber cutoff exists and is given by $k_{cutoff} \approx 22$. The most unstable mode is located at $k \simeq 6.54$ with $\mathrm{Re}\,(\sigma_+) \simeq 0.86$. (c) Graph of $\mathrm{Re}\,(\sigma_+)$ versus k along the section $F = 2.5$ in (a). Since $F > 1/\sqrt{\delta(1-\delta)}|_{\delta=3/8} \simeq 2.07$, a high-wavenumber cutoff does not exist. An ultraviolet catastrophe does not occur, since $R_E < \infty$, and the growth rate is bounded as $k \to \infty$. (d) Graph of $\mathrm{Re}\,(\sigma_+)$ versus k along the section $F = 2.075$ in 7(a). Since $F > 1/\sqrt{\delta(1-\delta)}|_{\delta=3/8} \simeq 2.07$, a high-wavenumber cutoff does not exist. Unlike in (c), the most unstable mode occurs at the finite wavenumber $k \simeq 31.3$ at which $\mathrm{Re}\,(\sigma_+) \simeq 3.4$.

Consequently, the interior limit of the stability boundary formally satisfies $\lim_{k \to 0^+} F_B\,(\nu, 3/8) = 1$ notwithstanding the fact $\mathrm{Re}\,(\sigma_+) = 0$ for $k = 0$ for all $F \geqslant 0$.

Figures 7(b) and 7(c) are graphs of $\mathrm{Re}\,(\sigma_+)$ versus k corresponding to sections in figure 7(a) along $F = 1.75$ and 2.5, respectively (which are values for which instability occurs and for which k_{cutoff} exists or does not exist, respectively). In figure 7(b), $k_{cutoff} \approx 22$, and the most unstable mode occurs for $k \approx 6.54$. Although it cannot be seen in figure 7(b), $\mathrm{Re}\,(\sigma_+)$ continues to decrease as k increases but reaches a minimum located at $k \simeq 234.8$ with an approximate value given by $\mathrm{Re}\,(\sigma_+)|_{k=234.8} \simeq -113.85$. For $k > 234.8$, $\mathrm{Re}\,(\sigma_+)$ increases and monotonically approaches its finite negative

limiting value as $k \to \infty$ (given below). In figure 7(c), Re(σ_+) increases monotonically as k increases but remains bounded as $k \longrightarrow \infty$, so there is no ultraviolet catastrophe (which does develop if $R_E \to \infty$ as shown below).

While a finite high-wavenumber cutoff is sufficient to ensure the most unstable mode occurs at a finite wavenumber, it is not necessary. Figure 7(d) is a graph of Re(σ_+) versus k corresponding to an extended section in figure 7(a) along $F = 2.075$. This value of F satisfies $F > 1/\sqrt{\delta(1-\delta)} \simeq 2.07$ ($\delta = 3/8$), so there is no high-wavenumber cutoff as occurs in figure 7(c). However, unlike the curve shown in figure 7(c), there is a most unstable mode located at $k \simeq 31.3$, where Re$(\sigma_+)|_{k=31.3} \simeq 3.4$. In figure 7($d$), as k increases after the maximum has been achieved, Re(σ_+) begins to decrease (of course) and approaches its finite positive limiting value as $k \to \infty$ (given below).

This behaviour is potentially physically important, since it implies that even though $F > 1/\sqrt{\delta(1-\delta)}$ the most unstable mode can occur at a finite wavenumber when turbulent horizontal dissipation is included in the dynamics. The boundary between the regions in which the most unstable mode has a finite wavenumber and in which the most unstable mode occurs for $k \to \infty$ is denoted by F_k and will satisfy

$$F_k(\delta, R_E, c_D) > 1/\sqrt{\delta(1-\delta)}$$

(it is understood $R_E < \infty$). That is when $F < F_k$ the most unstable mode occurs for $k < \infty$, and when $F > F_k$ the most unstable mode occurs for $k \to \infty$. Detailed calculations to determine F_k over the domain $\delta \in (0, 1)$ (for typical values of R_E and c_D) show F_k is sharply defined and only 'slightly' larger than $1/\sqrt{\delta(1-\delta)}$. Indeed, a graph of $F = F_k$ if included in figure 7(a) is all but completely indistinguishable from the graph of $F = 1/\sqrt{\delta(1-\delta)}$ and is therefore not included here (but is shown in figure 9a as described later in this section).

In summary, the global morphology of the graph of Re(σ_+) versus k as a function of F for finite R_E can be described as follows: For $0 < F < F_m$ (where the flow is asymptotically stable), Re(σ_+) decreases from zero (its value at $k=0$) and approaches a finite negative limiting value as $k \to \infty$ (not shown here). For $F_m < F < 1/\sqrt{\delta(1-\delta)}$, Re$(\sigma_+)$ initially increases from zero and reaches a positive maximum located at a finite value of k and subsequently decreases passing through zero at $k = k_{cutoff}$ and ultimately approaches a finite negative limiting value as $k \to \infty$ (as shown in figure 7b). As F increases through $1/\sqrt{\delta(1-\delta)}$, there will exist a finite $F_k > 1/\sqrt{\delta(1-\delta)}$ such that for $1/\sqrt{\delta(1-\delta)} < F < F_k$, Re$(\sigma_+)$ will increase from zero (its value at $k=0$) reaching a positive maximum located at a finite value of k and will subsequently decreaseapproaching a finite positive limiting value as $k \to \infty$ (as shown in figure 7c). For $F > F_k$, Re(σ_+) monotonically increases from zero and approaches a finite positive limiting value as $k \to \infty$ (as shown in figure 7d), and there is no most unstable mode located at a finite value of k (i.e. no local maximum in Re(σ_+)).

The asymptotic structure of Re(σ_+) for large k can be explicitly determined. If $R_E < \infty$, it follows from (3.3) the leading-order behaviour of σ_+ as $k \to \infty$ is given by

$$\sigma_+ \sim [\delta(1-\delta)F^2 - 1]R_E - \mathrm{i}(1-\delta)Fk + O(k^{-1}). \tag{3.29}$$

In figure 7(b) the range of k values in the graph is insufficient to show Re$(\sigma_+) \to -63.50$ (since $\delta = 3/8$, $F = 1.75$ and $R_E = 225$) as $k \to \infty$. However, in figure 7(c) it is seen Re$(\sigma_+) \to 104.59$ (since $\delta = 3/8$, $F = 2.5$ and $R_E = 225$) as $k \to \infty$. In figure 7(d), it is seen Re$(\sigma_+) \to 2.05$ (since $\delta = 3/8$, $F = 2.075$ and $R_E = 225$) as $k \to \infty$.

In the infinite-Reynolds-number limit, $R_E \to \infty$, the behaviour of σ_+ as $k \to \infty$ is determined as follows: The $R_E \to \infty$ limit of (3.3) is simply

$$\sigma_+ = -\mathrm{i}\,(1-\delta)\,Fk - c_D/F + \sqrt{(c_D/F)^2 + [\delta\,(1-\delta)\,F^2 - 1]k^2 - \mathrm{i}c_D k\,(1+2\delta)}.\quad(3.30)$$

Thus, if $\delta(1-\delta)F^2 > 1$, it follows from (3.30)

$$\sigma_+ \sim |k|\,[\sqrt{\delta\,(1-\delta)\,F^2 - 1} - \mathrm{i}\,(1-\delta)\,F] + O\,(1),\quad(3.31)$$

as $k \to \infty$, so $\mathrm{Re}\,(\sigma_+) \propto +|k|$, and an ultraviolet catastrophe develops. On the other hand, if $\delta(1-\delta)F^2 < 1$, it follows from (3.30), after a little algebra,

$$\sigma_+ \sim \frac{c_D[F^2\,(1+8\delta) - 4]}{2F\sqrt{1 - \delta\,(1-\delta)\,F^2}[(1+2\delta)\,F + 2\sqrt{1 - \delta\,(1-\delta)\,F^2}]}$$
$$- \mathrm{i}k[(1-\delta)\,F + \sqrt{1 - \delta\,(1-\delta)\,F^2}] + O\,(1/k),\quad(3.32)$$

as $k \to \infty$. Comparing (3.32) with (3.15), one sees if $F_m < F < 1/\sqrt{\delta(1-\delta)}$, then instability occurs, of course, but $\mathrm{Re}\,(\sigma_+)$ remains bounded as $k \to \infty$. Notwithstanding (3.32) has been derived in the $R_E \to \infty$ limit; comparing (3.32) with (3.22) suggests the relationship $\mathrm{Re}\,(\sigma_+) \sim k_{cutoff}^2/(2R_E)$ as $k \to \infty$ if $\delta(1-\delta)F^2 < 1$.

Within the context of $R_E \to \infty$, the boundary between the regions in which an ultraviolet catastrophe occurs and in which the growth rate is bounded (as $k \to \infty$) is given by $\delta(1-\delta)F^2 = 1$. On the boundary, it follows from (3.30)

$$\mathrm{Re}\,(\sigma_+) \sim \sqrt{c_D\,|k|\,(1+2\delta)\,/2},\quad(3.33)$$

as $k \to \infty$. Thus, while an ultraviolet catastrophe still develops on the boundary curve $\delta(1-\delta)F^2 = 1$, the growth rate exhibits sub-linear growth with respect to k.

Figures 8(a) and 8(b) are contour plots of the geostationary and co-moving frequency of the σ_+ root, denoted by ω and ω_{co}, respectively, and given by

$$\omega \equiv -\mathrm{Im}\,(\sigma_+) \quad \text{and} \quad \omega_{\mathrm{co}} \equiv \omega - Fk,\quad(3.34)$$

respectively, in the (k, F)-plane for same parameter values as in figure 7(a). The 'large' positive frequency seen in figure 8(a) is a consequence of the 'strong' doppler shift associated with the 'rapid' downslope overflow. Figure 8(b) shows the transition from prograde to retrograde propagation as the Froude number increases. Along the 0-contour in figure 8(b), the perturbation is stationary with respect to the background flow.

Figure 8(c) is a contour plot of the phase velocity

$$c = \omega/k,\quad(3.35)$$

associated with the σ_+ root in the (k, F)-plane for selected contours. The parameter values are as given in figure 7(a). Overall, there is little variability in c for the (k, F) domain shown. For $k \lesssim 10$, there is a gradual monotonic increase in c as F increases (for a fixed k). In the region $k \gtrsim 10$, c gradually increases as F initially increases from zero (for a fixed k). In the near region around $F \approx F_k \gtrsim 1/\sqrt{\delta(1-\delta)} \simeq 2.07$ ($\delta = 3/8$, i.e. the boundary between the regions in which the high-wavenumber cutoff k_{cutoff} is finite and in which it is not), c decreases slightly and then continues to gradually increase as F increases.
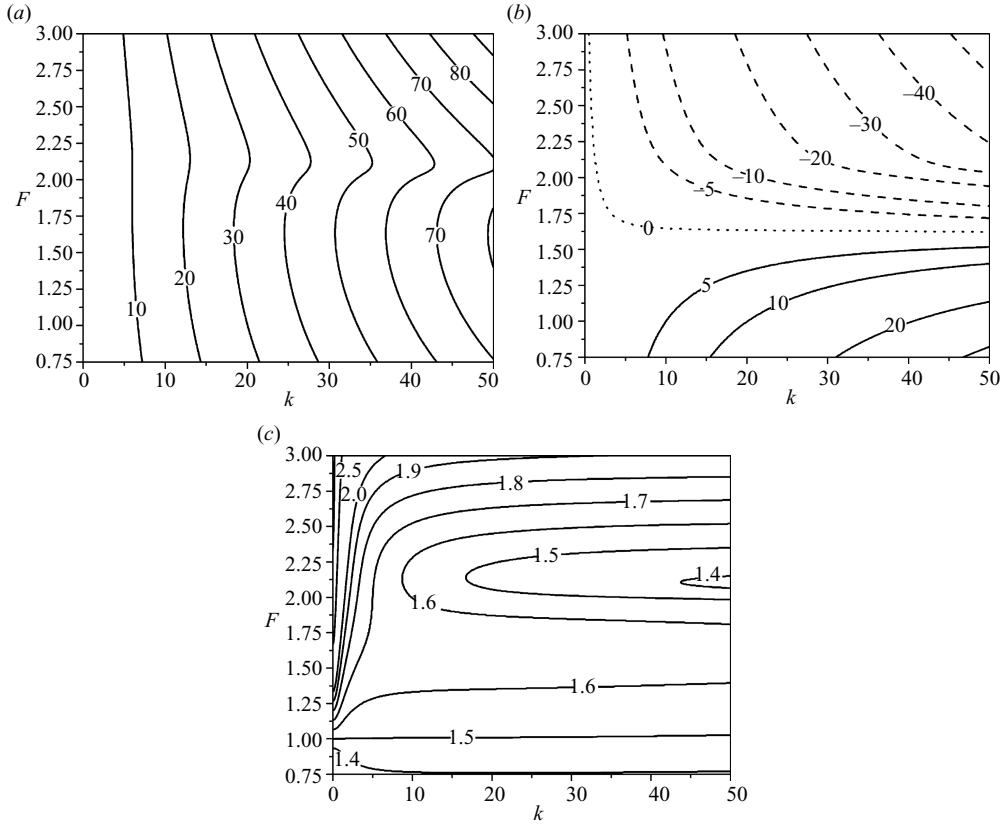
(a)

(b)

(c)

FIGURE 8. (a) Contour plot of the geostationary frequency $\omega = -\,\mathrm{Im}\,(\sigma_+)$ in the (k, F)-plane for selected contours. The parameter values are as given in figure 7(a). The 'large' positive frequency is a consequence of the doppler shift associated with the 'rapid' downslope overflow. Dimensionally, $\omega = 10$ corresponds to an oscillation period of about 7 hours; $F = 1$ corresponds to a downslope abyssal flow speed of about 37 cm s^{-1}; and $k = 10$ corresponds to a wavelength of about 9.4 km. (b) Contour plot of the co-moving frequency $\omega_{\mathrm{co}} = \omega - Fk$ in the (k, F)-plane for selected contours. The parameter values are as given in figure 7(a). The positive (negative) contours correspond to where the modes propagate prograde (retrograde) with respect to the background downslope flow. The 0-contour corresponds to where the mode is stationary with respect to the background overflow. (c) Contour plot of the phase velocity $c = \omega/k$ in the (k, F)-plane for selected contours. The parameter values are as given in figure 7(a). Dimensionally, $c = 1$ corresponds to a downslope phase velocity of about 37 cm s^{-1}.

3.2.1. *The most unstable mode*

The space–time characteristics of the most unstable modes are now described. The growth rate of the most unstable mode, denoted by σ_{max}, is defined by

$$\sigma_{max} = \max_k \left[\mathrm{Re}\,(\sigma_+)\right]. \qquad (3.36)$$

Since it is assumed that $R_E < \infty$, it follows $|\sigma_{max}| < \infty$. In addition, when $F < F_k$, it necessarily follows that

$$\sigma_{max} = \mathrm{Re}\,(\sigma_+)|_{k=k_{max}}, \quad \text{where} \quad \left.\frac{\partial\,\mathrm{Re}\,(\sigma_+)}{\partial k}\right|_{k=k_{max}} = 0, \qquad (3.37)$$
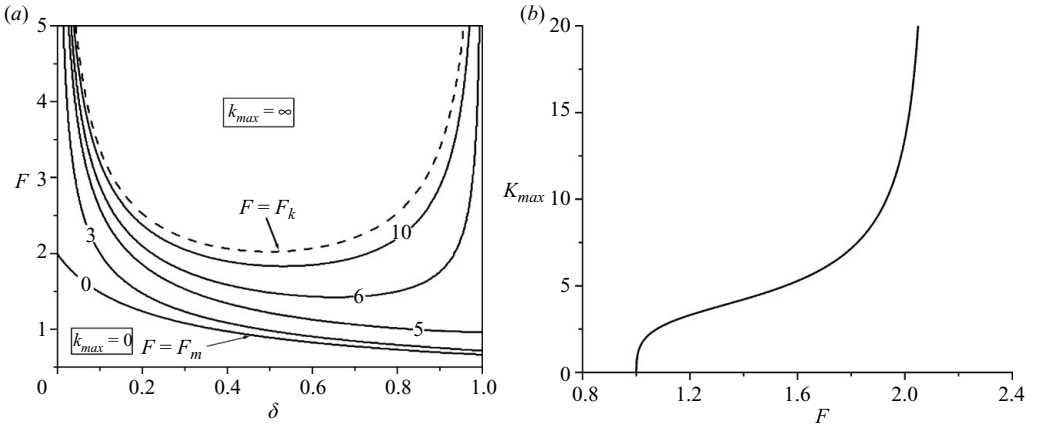
FIGURE 9. (a) Contour plot of the wavenumber of the most unstable mode k_{max} in the (δ, F)-plane for selected contours (with $c_D = 1.0$ and $R_E = 225.0$). The 0-contour is the marginal stability boundary $F = F_m$. In the region $F \leqslant F_m$, the flow is stable, and the 'most unstable mode' has $k_{max} = 0 \Longrightarrow \sigma_{max} = 0$. The boundary between the regions in which $k_{max} < \infty$ and $k_{max} \to \infty$ is the dashed curve $F = F_k$. Dimensionally, $k_{max} = 1$ corresponds to a wavelength of about 94 km, and $F = 1$ corresponds to a downslope abyssal flow speed of about 37 cm s^{-1}. (b) Graph of k_{max} versus F along the section $\delta = 3/8$ in (a).

where k_{max} is the finite wavenumber associated with the most unstable mode. When $F \geqslant F_k$, the most unstable mode has a finite growth rate that, however, occurs at infinite wavenumber, i.e. $k_{max} \to \infty$ (where, formally, the modelling assumptions required for shallow-water theory are violated). When the flow is stable, i.e. $F \leqslant F_m$, it follows that $k_{max} = 0$ (as shown above). The geostationary frequency and phase velocity of the most unstable mode will be denoted by ω_{max} and c_{max}, respectively, and are given by, respectively,

$$\omega_{max} \equiv -\operatorname{Im}(\sigma_+)|_{k=k_{max}} \text{ and } c_{max} = \frac{\omega_{max}}{k_{max}}, \tag{3.38}$$

where it is understood that the formula for c_{max} must be replaced with the appropriate limit if $k_{max} = 0$ or $k_{max} \to \infty$.

Figure 9(a) is a contour plot of k_{max} in the (δ, F)-plane for selected contours (with $c_D = 1.0$ and $R_E = 225.0$). The 0-contour is the marginal stability boundary $F = F_m$. In the region $F \leqslant F_m$, the flow is stable, and the 'most unstable mode' has $k_{max} = 0 \Longrightarrow \sigma_{max} = 0$, which follows from (3.3). The boundary between the regions in which $k_{max} < \infty$ and $k_{max} \to \infty$ is the dashed curve $F = F_k$. It can be seen in figure 9(a) that, for fixed δ, k_{max} is an increasing function of the Froude number in the interval $F_m < F < F_k$.

The qualitative behaviour of k_{max} versus δ for a fixed value of F is more complicated to describe. For $2/3 = F_m|_{\delta=1} < F < F_m|_{\delta=0} = 2$, k_{max} is an increasing function of δ in the interval $\delta \in (\delta_m, 1)$, where

$$\delta_m \equiv [(2/F)^2 - 1]/8, \tag{3.39}$$

as determined from (3.16), except for a small region of values $(\delta, F) \approx (1^-, F_m|_{\delta=0})$ in which k_{max} begins to decrease. For $F_m|_{\delta=0} < F < \min_\delta[F_k]$, k_{max} initially increases as δ increases from zero, but a finite maximum is reached (at about $\delta \gtrsim 1/2$), and then k_{max} decreases as $\delta \to 1^-$. If $F > \min_\delta[F_k]$, k_{max} initially increases as δ increases from zero and becomes unbounded as the left-hand branch of the curve $F = F_k$ is
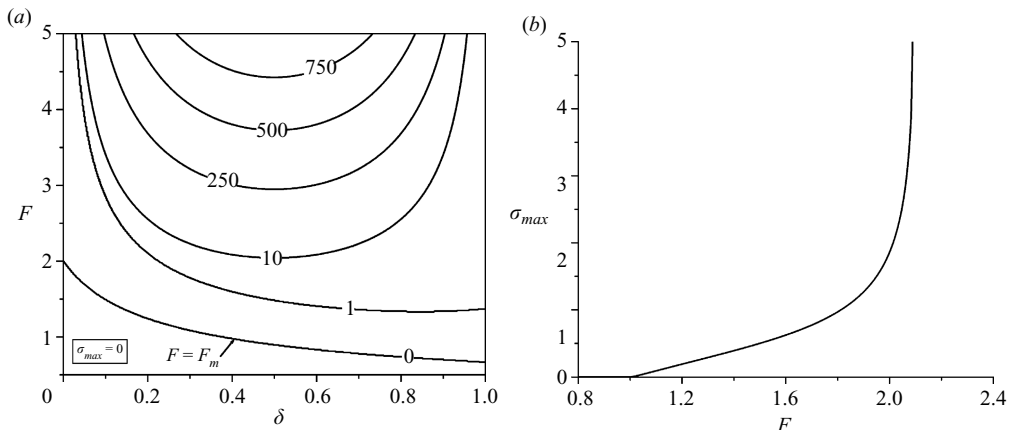
FIGURE 10. (*a*) Contour plot of the growth rate of the most unstable mode σ_{max} in the (δ, F)-plane for selected contours (with c_D and R_E as given in figure 9*a*). The 0-contour is the marginal stability boundary $F = F_m$. In the region $F \leqslant F_m$, $\sigma_{max} = 0$. The curve $F = F_k$ (see figure 9*a*) and the 10-contour are essentially indistinguishable. Dimensionally, $\sigma_{max} = 1$ corresponds to an e-folding amplification time of about 11 hours, and $F = 1$ corresponds to a downslope abyssal flow speed of about 37 cm s^{-1}. (*b*) Graph of σ_{max} versus F along the section $\delta = 3/8$ in (*a*).

intersected, remains unbounded until the right-hand branch of the curve $F = F_k$ is intersected, whereupon k_{max} is again finite, and thereafter it decreases as $\delta \to 1^-$.

For Froude numbers in the unstable interval $F_m < F < F_k$ (where $k_{max} < \infty$), a representative value for k_{max} is about 5. Based on the 'topographic length scale' of about 15 km introduced in §2, figure 9(*a*) suggests that the most unstable mode associated with the mixed frictional–KH instability described here would have a dimensional wavelength of the order of about 19 km.

Figure 9(*b*) is a graph of k_{max} versus F corresponding to a section along $\delta = 3/8$ (characteristic of the DSO) in figure 9(*a*). For $0 \leqslant F \leqslant F_m|_{\delta = 3/8} = 1$, $k_{max} = 0$. In the region $F_m|_{\delta = 3/8} < F < F_k \approx 2.07$, k_{max} monotonically increases as F increases. There is a vertical asymptote at $F = F_k$ for which $\lim_{F \to F_k^-} k_{max} = \infty$ and $k_{max} = \infty$ for all $F > F_k$.

Figure 10(*a*) is a contour plot of the growth rate of the most unstable mode, σ_{max}, in the (δ, F)-plane for selected contours (with c_D and R_E as in figure 9). As in figure 9(*a*), the 0-contour is the marginal stability boundary $F = F_m$. In the region $F \leqslant F_m$, $\sigma_{max} = 0$. While not mathematically identical, the curve $F = F_k$ is indistinguishable from the 10-contour in figure 10(*a*). Figure 10(*a*) shows that, for fixed δ, σ_{max} is an increasing, but nevertheless bounded, function of the Froude number when $F > F_m$.

Again, the qualitative behaviour of σ_{max} versus δ for a fixed value of F is more complicated to describe. For $F_m|_{\delta = 1} < F < F_m|_{\delta = 0}$, σ_{max} is an increasing function of δ in the interval $\delta \in (\delta_m, 1)$, except for a small region of values $(\delta, F) \approx (1^-, F_m|_{\delta = 0})$ in which σ_{max} begins to decrease. For $F > F_m|_{\delta = 0}$, σ_{max} initially increases as δ increases from zero until a finite maximum is reached, and then σ_{max} decreases as $\delta \to 1^-$.

For the interval $F_m < F < F_k$, a representative value for σ_{max} is about 5. Based on the 'topographic time scale' of about 11 hours introduced in §2, figure 10(*a*) suggests that the most unstable mode would have dimensional e-folding amplification time scale of the order of about 2 hours. In the region $F > F_k$ in figure 10(*a*), σ_{max} increases quadratically as F increases (note that it follows from (3.29) that
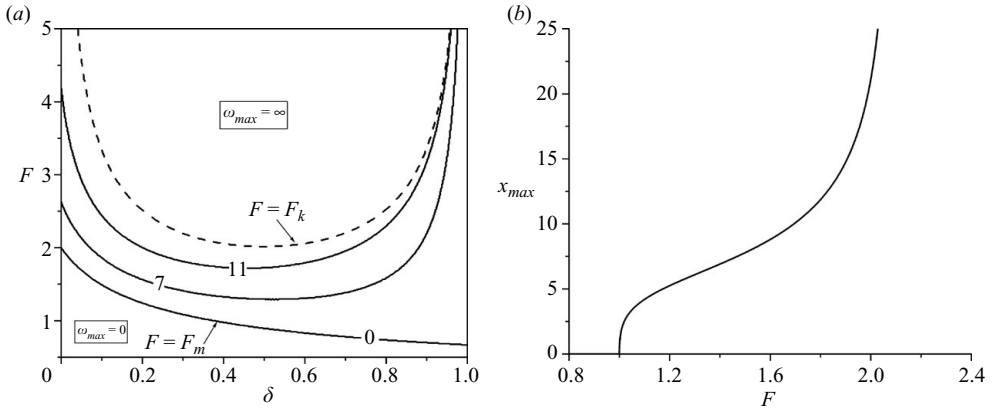
FIGURE 11. (a) Contour plot of the geostationary frequency of the most unstable mode ω_{max} in the (δ, F)-plane for selected contours (with c_D and R_E as given in figure 9a). The 0-contour is the marginal stability boundary $F = F_m$. In the region $F \leqslant F_m$, $\omega_{max} = 0$. The curve $F = F_k$ is the boundary between the regions in which $\omega_{max} < \infty$ and $\omega_{max} \to \infty$. Dimensionally, $\omega_{max} = 10$ corresponds to an oscillation period of about 7 hours, and $F = 1$ corresponds to a downslope abyssal flow speed of about 37 cm s^{-1}. (b) Graph of ω_{max} versus F along the section $\delta = 3/8$ in (a).

$\sigma_{max} \simeq [\delta(1 - \delta)F^2 - 1]R_E)$. Note that σ_{max} is proportional to R_E in the region $F > F_k$. Thus, as argued previously, in the $R_E \to \infty$ limit, the theory presented here implies that an ultraviolet catastrophe develops in the region $F > F_k$ in the infinite R_E limit.

Figure 10(b) is a graph of σ_{max} versus F corresponding to a section along $\delta = 3/8$ in figure 10(a). For $0 \leqslant F \leqslant F_m|_{\delta = 3/8}$, $\sigma_{max} = 0$. In the region $F > F_m|_{\delta = 3/8}$, σ_{max} monotonically increases but remains continuous as F increases. Although figure 10(b) seems to suggest it, there is no vertical asymptote at $F = F_k$.

Figure 11(a) is a contour plot of ω_{max} in the (δ, F)-plane for selected contours (with c_D and R_E as in figure 9). Again, the 0-contour is the marginal stability boundary $F = F_m$, and the dashed line is the curve $F = F_k$. In the region $F \leqslant F_m$, $\omega_{max} = 0$. Since $\omega_{max} = \sigma_{max} = 0$ along the marginal stability curve $F = F_m$, this stability problem exhibits the principle of 'exchange of stability' (Drazin & Reid 1981). The qualitatively behaviour of ω_{max} in the (δ, F)-plane (as opposed to the quantitative values) is more or less identical to the qualitative behaviour of k_{max} and is thus not reproduced here.

For the interval $F_m < F < F_k$, a representative value for ω_{max} is about 5. Based on the scalings introduced in §2, figure 11(a) suggests that the most unstable mode would have dimensional period of the order of about 14 hours. The curve $F = F_k$ separates the regions in which $\omega_{max} < \infty$ from those in which $\omega_{max} \to \infty$. Note that it follows from (3.29) that $\omega_{max} \to \infty$, since $k_{max} \to \infty$ in the region $F > F_k$.

Figure 11(b) is a graph of ω_{max} versus F corresponding to a section along $\delta = 3/8$ in figure 11(a). For $0 \leqslant F \leqslant F_m|_{\delta = 3/8}$, $\omega_{max} = 0$. In the region $F_m|_{\delta = 3/8} < F < F_k$, ω_{max} monotonically increases as F increases. There is a vertical asymptote at $F = F_k$ for which $\lim_{F \to F_k^-} \omega_{max} = \infty$ and $\omega_{max} = \infty$ for all $F > F_k$.

Figure 12(a) is a contour plot of c_{max} in the (δ, F)-plane for selected contours (with c_D and R_E as in figure 9). In the regions $0 < F \leqslant F_m$ and $F \geqslant F_k$, where $k_{max} = \omega_{max} = 0$ and $k_{max} = \omega_{max} = \infty$, respectively, c_{max} is formally computed as the limit

$$c_{max} = \lim_{k \to 0} \frac{\omega}{k} \quad \text{and} \quad c_{max} = \lim_{k \to \infty} \frac{\omega}{k}, \tag{3.40}$$
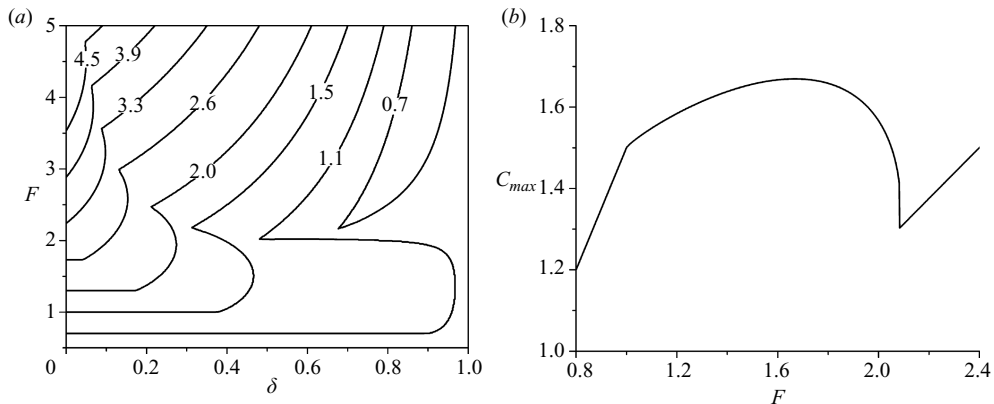
FIGURE 12. (a) Contour plot of the phase velocity of the most unstable mode c_{max} in the (δ, F)-plane for selected contours (with c_D and R_E as given in figure 9a). Dimensionally, $c_{max} = 1$ corresponds to a phase velocity of about 37 cm s^{-1}, and $F = 1$ corresponds to a downslope abyssal flow speed of about 37 cm s^{-1}. (b) Graph of c_{max} versus F along the section $\delta = 3/8$ in (a).

respectively (holding δ and F fixed). The resulting c_{max} will be a smooth function of the variables (δ, F) everywhere except across the curves $F = F_m$ and $F = F_k$. Across these curves, c_{max} will be continuous but not differentiable. This explains the 'corners' in figure 12(b), which is a graph of c_{max} versus F corresponding to a section along $\delta = 3/8$ in figure 12(a), that are located at $F = F_m$ and $F = F_k$, respectively. The loss of smoothness in c_{max} across the curves $F = F_m$ and $F = F_k$ can also be seen in figure 12(a). A 'typical' value of c_{max} in figure 12(a) is about 2. Based on the scalings introduced in §2, figure 12(a) suggests that the most unstable mode would have *dimensional* downslope phase speed of the order of about 74 cm s^{-1}.

4. Effects of mean depth variations in the upper layer

In the $R_E \to \infty$ limit, the linear stability equation (2.26) may be written in the form

$$\left[(1 - \delta)(\partial_t + F\partial_x)^2 + (2c_D/F)(\partial_t + F\partial_x) - \partial_{xx} + c_D\partial_x + \frac{\delta}{1 + sx}\partial_{tt}\right]\phi = 0, \quad (4.1)$$

where ϕ is the downslope mass transport in the upper layer, given by

$$\phi \equiv (1 + sx)u_1. \quad (4.2)$$

Since the coefficient $1 + sx$ in (4.1) is, in fact, the mean depth of the upper layer with the linearly sloping bottom included (see figure 1), it is required on physical grounds that $1 + sx \geqslant 0$. That is the depth of the upper layer is never negative. In turn, this implies that the spatial domain is the semi-infinite interval $x > -1/s$ (it is assumed that $s > 0$; see figure 1 and (2.18)). Of course, from the viewpoint of modelling baroclinic grounded abyssal overflows in the ocean, it is to be expected that the depth of the overlying water column is never remotely near zero. This and $s \simeq 0.4$ (see §2) suggest the physical relevancy of the $s = 0$ stability problem as examined in §3. Nevertheless, it is of interest to examine the stability problem when variations in the mean upper depth are retained. In particular, because of the order of magnitude of s, determining the geometrical optics correction associated with retaining the sx contribution in (4.1) under a 'slowly varying approximation' is physically relevant.

The principal purpose of this section to describe aspects of the stability problem (in the $R_E \to \infty$ limit) when mean depth variations are retained in the upper layer.

4.1. *Classification of the linear stability operator*

Before proceeding further it is instructive to point out some properties associated with (4.1). The $\delta = 0$ limit of (4.1) is the reduced gravity approximation and corresponds to the classical stability equation associated with roll-wave formation down an inclined plane (see, e.g., §3.2 in Whitham 1974). The $s = 0$ limit of (4.1) gives rise to the $R_E \to \infty$ limit of the dispersion relation (3.3), the σ_+ solution of which is given by (3.30). As shown in §3.2, if $F \geqslant 1/\sqrt{\delta(1-\delta)}$, then an ultraviolet catastrophe develops, and if $0 < F < 1/\sqrt{\delta(1-\delta)}$, the growth rate of the unstable modes remains bounded for all k.

The stability characteristics of the $s = 0$ dispersion relation are a consequence of the fact that the second-order partial differential operator in (4.1) is elliptic for $|F|\sqrt{\delta(1-\delta)} > 1$, so the stability index will be $+\infty$, implying ill posedness and the ultraviolet catastrophe. The characteristic curves in the (x, t)-plane associated with (4.1) (with $s > 0$) are determined by

$$\frac{dx}{dt}\bigg|_{characteristics} = \frac{F(1-\delta)(1+sx) \pm \sqrt{(1+sx)\left[1 + (1-\delta)sx - \delta(1-\delta)F^2\right]}}{1 + (1-\delta)sx}. \quad (4.3)$$

If $s = 0$, (4.3) implies that (4.1) is hyperbolic, parabolic and elliptic for $|F|\sqrt{\delta(1-\delta)} < 1$, $|F|\sqrt{\delta(1-\delta)} = 1$ and $|F|\sqrt{\delta(1-\delta)} > 1$, respectively.

If $s > 0$, (4.1) has, potentially, a spatially dependent classification in the domain $x > -1/s$, which is determined by the sign of $\mathscr{D}$, given by,

$$\mathscr{D} \equiv 1 + (1-\delta)sx - \delta(1-\delta)F^2. \quad (4.4)$$

Observing that

$$\mathscr{D}|_{x=-1/s} = \delta[1 - (1-\delta)F^2]$$

and appreciating that $\mathscr{D}$ increases linearly with respect to x implies that if $(1-\delta)F^2 < 1$, then (4.1) is strictly hyperbolic for all $x > -1/s$.

On the other hand, if $(1-\delta)F^2 \geqslant 1$, then (4.1) is elliptic for $x \in (-1/s, X_*)$, where X_* is given by

$$X_* \equiv \frac{\delta(1-\delta)F^2 - 1}{(1-\delta)s} = -\frac{1}{s} + \frac{\delta\left[(1-\delta)F^2 - 1\right]}{(1-\delta)s}, \quad (4.5)$$

and is strictly hyperbolic for $x > X_*$. Formally, (4.1) is parabolic at the transition point $x = X_*$. It follows from (2.8) and (2.14) that

$$(1-\delta)F^2 = \frac{U^2}{g'h_*},$$

which is the square of the Froude number for the abyssal flow based on the long gravity wave speed in the reduced gravity limit.

4.2. *An exact solution*

There is an exact solution to (4.1) valid for the entire domain $x > -1/s$ that satisfies the no normal mass flux boundary condition $\phi(-1/s, t) = 0$ for all $t > 0$, which reduces to the normal mode solution obtained in §3 for $s \to 0^+$. Introducing the normal mode decomposition

$$\phi(x, t) = \exp(\sigma t - \alpha x/2)\, \Phi(x) + \text{c.c.}, \quad (4.6)$$

where σ is the complex-valued growth rate and

$$\alpha \equiv \frac{2\sigma\,(1-\delta)\,F + 3c_D}{(1-\delta)\,F^2 - 1}, \tag{4.7}$$

into (4.1) leads to

$$\Phi_{xx} + \left(\frac{4\beta - \alpha^2}{4} + \frac{\gamma}{1+sx}\right)\Phi = 0, \tag{4.8}$$

where

$$\beta \equiv \frac{(1-\delta)\,\sigma^2 + 2c_D\sigma/F}{(1-\delta)\,F^2 - 1} \text{ and } \gamma \equiv \frac{\delta\sigma^2}{(1-\delta)\,F^2 - 1}. \tag{4.9}$$

Equation (4.9) can be put into canonical form via the change of variable

$$\xi \equiv \sqrt{\mu}\,(1+sx)/s \text{ with } \mu \equiv \alpha^2 - 4\beta$$

$(x > -1/s \Longleftrightarrow \xi > 0 \text{ since } s > 0)$, leading to

$$\Phi_{\xi\xi} + \left(-\frac{1}{4} + \frac{\kappa}{\xi}\right)\Phi = 0, \text{ where } \kappa \equiv \frac{\gamma}{s\sqrt{\mu}}. \tag{4.10}$$

Equation (4.10) is a reduced Whittaker equation (Abramowitz & Stegun 1970). The solution to (4.10) for which the upper layer downslope velocity u_1 is bounded at $\xi = 0$ can be written in the form

$$\Phi = A\xi \exp(-\xi/2)\,M(1-\kappa,\,2,\,\xi), \tag{4.11}$$

where A is a free amplitude coefficient and $M(1-\kappa,\,2,\,\xi)$ is the Kummer function of the first kind (Abramowitz & Stegun 1970). Substitution of (4.11) into (4.6) leads to

$$\phi(x,\,t) = \widetilde{A}\,(1+sx)\exp[\sigma t - (\alpha + \sqrt{\alpha^2 - 4\beta})x/2]$$
$$\times M\left[1 - \frac{\gamma}{s\sqrt{\alpha^2 - 4\beta}},\,2,\,\frac{(1+sx)\sqrt{\alpha^2 - 4\beta}}{s}\right] + \text{c.c.}, \tag{4.12}$$

where $\widetilde{A}$ is a free amplitude constant.

Figure 13 is a graph of $\phi(x,\,0)$ versus x for $x \in (-1/s,\,-1/s + 20\pi/k)$ as determined by (4.12) with $c_D = 1.0$, $F = 1.5$, $\delta = 3/8$, $s = 0.4$ and $\sigma \simeq 0.55 - 8.27\mathrm{i}$ (which follows from (3.3) with $k = 5$ and $R_E \to \infty$). These parameter values roughly correspond to the DSO. From figure 9(a), $k = 5$ is characteristic of k_{max} for $F = 1.5$ and $\delta = 3/8$ (although $R_E = 225$ in figure 9a). Since $F_m|_{\delta=3/8} < F < 1/\sqrt{\delta(1-\delta)}|_{\delta=3/8}$, these parameter values give rise to an unstable mode for which the growth rate is bounded for all wavenumbers in the $s = 0$ stability theory. The free amplitude coefficient $\widetilde{A}$ has been chosen so that $\max|\phi(x,\,0)| \simeq 1$.

Dimensionally, the unstable mode shown in figure 13 has a e-folding amplification time of the order of about 20 hours and a period of about 8.4 hours. The x-interval being plotted equals 10 wavelengths associated with the corresponding unstable mode in the $s = 0$ theory (given by about 19 km). Figure 13 shows that there are about nine oscillation cycles in the spatial domain being plotted, suggesting that while the oscillatory structure associated with (4.12) is obviously no longer monochromatic, on average the wavelength is remarkably close to the the predictions of the $s = 0$ stability theory. Spatially, the envelope amplitude in $\phi(x,\,0)$ is seen to increase rapidly from zero at $x = -1/s = -2.5$, reaching a maximum at about $x \simeq 1.25$ or equivalently, dimensionally about 56 km downslope from $x = -1/s$ and then subsequently gradually
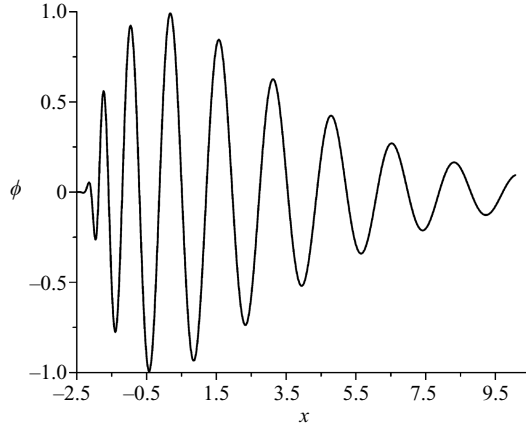
FIGURE 13. Graph of $\phi(x, 0)$ versus x for $x \in (-1/s, -1/s+20\pi/k)$ as determined by the exact solution (4.12) with $c_D = 1.0$, $F = 1.5$, $\delta = 3/8$, $s = 0.4$ and $\sigma \simeq 0.55 - 8.27i$ (which follows from (3.3) with $k = 5$ and $R_E \to \infty$). The amplitude coefficient $\widetilde{A}$ has been chosen so that $\max |\phi(x, 0)| \simeq 1$. Dimensionally, 1 unit along the x-axis corresponds to about 15 km.

decreasing towards zero as x further increases, which is accompanied by a progressive stretching of the wavelength of the oscillations. Overall, figure 13 suggests that for oceanographically relevant parameter values, the gross features of the unstable modes are well described by the $s = 0$ stability theory with the effects of upper layer depth variations introducing geometrical optics corrections to the amplitude and oscillation wavelength. This theory will be presented later in this section.

In principle, (4.12) and the Laplace transform can be used to solve (at least to within quadrature) the initial-value problem for (4.1) for arbitrary initial data. However, this representation for the solution to the initial-value problem is not particularly enlightening and is not pursued. An interpretative difference between (4.12) and (3.2) is that in (4.12) the 'wavenumber' may be considered a function of the 'growth rate', whereas in (3.2) the growth rate is a function of the wavenumber. In the remaining two sub-sections, it is shown how the $\delta \to 0^+$ and $s \to 0^+$ limits of (4.12) reduce to the normal mode solutions obtained in §3.

4.2.1. *The $\delta = 0$ limit of the exact solution*

The $\delta = 0$ limit (i.e. the reduced gravity limit in which the upper layer is infinitely deep and dynamically inactive) of (4.12) must correspond to the normal mode solution obtained in §3 (i.e. (3.2) and (3.3) with $\delta = 0$ and $R_E \to \infty$). Moreover, since the $\delta = 0$ limit implies that there is no longer any s dependence in (4.1), this dependence must completely drop out of (4.12) as $\delta \to 0$. Substituting $\delta = 0$ into (4.12) leads to

$$\phi(x, t)|_{\delta=0} = \widetilde{A}(1 + sx) \exp\left[\sigma t - \left(\alpha_0 + \sqrt{\alpha_0^2 - 4\beta_0}\right)x/2\right]$$
$$\times M\left[1, 2, (1 + sx)\sqrt{\alpha_0^2 - 4\beta_0}/s\right] + \text{c.c.}, \tag{4.13}$$

where

$$\alpha_0 = \alpha|_{\delta=0} = \frac{2\sigma F + 3c_D}{F^2 - 1}, \beta_0 = \beta|_{\delta=0} = \frac{\sigma(\sigma + 2c_D/F)}{F^2 - 1} \text{ and } \gamma|_{\delta=0} = 0. \tag{4.14}$$

However, it is known (see, e.g., equation (13.6.14) in Abramowitz & Stegun 1970) that

$$
M\left[1, 2, (1 + sx)\sqrt{\alpha_0^2 - 4\beta_0}/s\right]
$$
$$
= \frac{2s \exp\left[(1 + sx)\sqrt{\alpha_0^2 - 4\beta_0}/(2s)\right] \sinh\left[(1 + sx)\sqrt{\alpha_0^2 - 4\beta_0}/(2s)\right]}{(1 + sx)\sqrt{\alpha_0^2 - 4\beta_0}},
$$

so that

$$
\phi|_{\delta=0} = \widehat{A} \exp\left(\sigma t - \alpha_0 x/2\right)\left[\exp\left(x\sqrt{\alpha_0^2 - 4\beta_0}/2\right) - \exp\left(-x\sqrt{\alpha_0^2 - 4\beta_0}/2\right)\right], \quad (4.15)
$$

where $\widehat{A}$ is a free amplitude constant. Each of the two terms in (4.15) corresponds to a normal mode solution of the form (3.2) and (3.3) with $\delta = 0$ and $R_E \to \infty$.

This can be seen as follows: First, spatial (possibly complex-valued) wavenumbers $k_\pm$ are introduced, defined by

$$
ik_\pm \equiv \frac{-\alpha_0 \pm \sqrt{\alpha_0^2 - 4\beta_0}}{2} \implies k_\pm^2 - ik_\pm \alpha_0 = \beta_0.
$$

Substituting in for α_0 and β_0 using (4.14) yields a quadratic equation for σ, the solution of which is given by

$$
\sigma = -iFk_\pm - \frac{c_D}{F} \pm \sqrt{\left(\frac{c_D}{F}\right)^2 - k_\pm^2 - ic_D k_\pm},
$$

which is exactly (3.3) with $\delta = 0$ and $R_E \to \infty$ with $k = k_\pm$. Thus, both terms in (4.15) can be identified as normal mode solutions of the form (3.2) and (3.3) in the appropriate parameter limit constructed to satisfy $\phi(0, t) = 0$.

4.2.2. *The $s \to 0$ limit of the exact solution*

The $s \to 0^+$ limit of (4.12) must correspond to the normal mode solution obtained in §3 (i.e. (3.2) and (3.3) with $R_E \to \infty$) valid for $\delta \in (0, 1)$ and $x \in (-\infty, \infty)$. The most straightforward way to determine the structure of (4.12) in the limit $s \to 0^+$ is to work with an integral representation of Kummer's function. It is known (see, e.g., equation (13.2.1) in Abramowitz & Stegun 1970) that

$$
M(a, 2, z) = \frac{1}{\Gamma(2 - a)\Gamma(a)} \int_0^1 \exp(z\zeta)\left(\frac{1 - \zeta}{\zeta}\right)^{1-a} d\zeta. \quad (4.16)
$$

Employing (4.16) in (4.12) implies

$$
\phi = \overline{A}(1 + sx)\exp[\sigma t - (\alpha + \sqrt{\mu})x/2] \int_0^1 \exp\left[\sqrt{\mu}x\zeta + \frac{1}{s}\Phi(\zeta)\right] d\zeta, \quad (4.17)
$$

with

$$
\Phi(\zeta) \equiv \sqrt{\mu}\zeta + \frac{\gamma}{\sqrt{\mu}}\log\left[(1 - \zeta)/\zeta\right], \quad (4.18)
$$

where $\overline{A}$ is a free amplitude constant; $\mu \equiv \alpha^2 - 4\beta$; and the principal value is taken for the possibly complex-valued log function.

In the limit $s \to 0^+$ the dominant contribution to the integral in (4.17) comes from the points of stationary phase. Moreover, since the points of stationary phase are independent of x, the contributions that arise from the curvature terms associated with $\Phi(\zeta)$ (when it is Taylor expanded about the points of stationary phase) do not

have any spatial dependence and thus can be absorbed, without loss of generality, into the free amplitude constant $\overline{A}$.

The points of stationary phase are given by

$$\Phi'(\zeta) = 0 \implies \zeta = \zeta_{\pm} \equiv \frac{1 \pm \sqrt{1 - 4\gamma/\mu}}{2}. \tag{4.19}$$

It follows, therefore, that as $s \to 0^+$,

$$\begin{aligned}
\phi|_{s\to 0^+} &\simeq \exp\left[\sigma t - (\alpha + \sqrt{\mu})x/2\right]\left[\overline{A}_1 \exp(\sqrt{\mu}x\zeta_+) + \overline{A}_2 \exp(\sqrt{\mu}x\zeta_-)\right] \\
&= \exp\left(\sigma t - \frac{\alpha x}{2}\right)\left[\overline{A}_1 \exp\left(\frac{x}{2}\sqrt{\alpha^2 - 4(\beta + \gamma)}\right)\right. \\
&\quad \left. + \overline{A}_2 \exp\left(-\frac{x}{2}\sqrt{\alpha^2 - 4(\beta + \gamma)}\right)\right],
\end{aligned} \tag{4.20}$$

where $\mu \equiv \alpha^2 - 4\beta$; (4.9) has been used; and $\overline{A}_{1,2}$ are free amplitude coefficients. It is noted that $\Phi''(\zeta_{\pm}) = \mp(\mu/\gamma)\sqrt{\mu - 4\gamma}$.

Both terms in (4.20) individually correspond to normal mode solutions of the form (3.2) and (3.3) defined for $x \in (-\infty, \infty)$. As before, spatial wavenumbers $k_{\pm}$ are introduced, defined by

$$ik_{\pm} \equiv \frac{-\alpha \pm \sqrt{\alpha^2 - 4(\beta + \gamma)}}{2} \implies k_{\pm}^2 - ik_{\pm}\alpha = \beta + \gamma. \tag{4.21}$$

Substituting for α, β and γ using (4.7) and (4.9) yields a quadratic equation for σ, the solution of which is exactly (3.3) with $R_E \to \infty$ and $k = k_{\pm}$.

4.3. Geometrical optics solution

As previously discussed, from the perspective of the flow of grounded dense water over deep sills in the ocean it is of interest to determine the geometrical optics solution to (4.1) for a normal mode for which $0 < s \ll 1$. The purpose of this subsection is to obtain such a solution with the properties that it reduces to the $R_E \to \infty$ limit of (3.1)–(3.3) when $s \to 0$ and is uniformly valid (to the leading order) with respect to x.

Substitution of

$$\phi(x, t) = A \exp(\sigma t + ikx)\Phi(\xi) + \text{c.c.}, \tag{4.22}$$

into (4.1) where it is assumed that

$$k^2 - ik\alpha - \beta - \gamma = 0, \tag{4.23}$$

with $\xi \equiv sx$, A is a free amplitude constant and α, β and γ are given by (4.7) and (4.9), leads to

$$s^2 \Phi_{\xi\xi} + s(\alpha + 2ik)\Phi_{\xi} - \frac{\gamma\xi}{1 + \xi}\Phi = 0. \tag{4.24}$$

Again, it is remarked that substituting α, β and γ using (4.7) and (4.9) into (4.23) yields a quadratic equation for σ, the solution of which is exactly (3.3) with $R_E \to \infty$. The form of the solution (4.22) implies that $\Phi(\xi)$ describes *only* the spatial modulation of the otherwise monochromatic normal mode due to upper layer mean depth variations that arise due to the sloping bottom. Thus, without loss of generality, $\Phi(\xi) \to 1$ as ξ or $s \to 0$ may be imposed.

The geometrical optics solution to (4.24) valid in the limit $0 < s \ll 1$ can be written in the form

$$\Phi(\xi) = \psi(\xi) \exp\left[\frac{1}{s}\int_0^{\xi} \varphi(\eta)\,d\eta\right]. \tag{4.25}$$

Substitution of (4.25) into (4.24) leads to the leading- and first-order problems given by, respectively,

$$\varphi^2 + (\alpha + 2ik)\,\varphi - \frac{\gamma\xi}{1+\xi} = 0, \tag{4.26}$$

$$(2\varphi + \alpha + 2ik)\,\psi_\xi + \varphi_\xi\psi = 0, \tag{4.27}$$

which have the solutions

$$\varphi(\xi) = (ik + \alpha/2)\,[\Gamma(\xi) - 1], \tag{4.28}$$

$$\psi(\xi) = 1/\sqrt{\Gamma(\xi)}, \tag{4.29}$$

where

$$\Gamma(\xi) \equiv \sqrt{\frac{1 + \rho\xi}{1 + \xi}} \text{ with } \rho \equiv 1 + \frac{\gamma}{(ik + \alpha/2)^2} = \frac{\alpha^2 - 4\beta}{\alpha^2 - 4(\beta + \gamma)} = \frac{\mu}{\mu - 4\gamma}, \tag{4.30}$$

where (4.23) has been used. It is remarked that the free integration constant associated with integrating (4.27) has been chosen, without loss of generality, so $\psi(0) = 1$. Additionally, the '+' root associated with (4.28) is chosen to ensure $\varphi(0) = 1$.

Hence, the geometrical optics solution to (4.1), valid in the limit $0 < s \ll 1$, can be written in the form

$$\phi(x, t) = \frac{A}{\sqrt{\Gamma(sx)}} \exp\left[\sigma t - \alpha x/2 + \frac{(ik + \alpha/2)}{s} \int_0^{sx} \Gamma(\xi)\,d\xi\right] + \text{c.c.}. \tag{4.31}$$

Note, that as constructed

$$\lim_{s \to 0} \frac{1}{s} \int_0^{sx} \Gamma(\xi)\,d\xi = x, \tag{4.32}$$

so that (4.31) reduces exactly to the normal mode solution (3.1)–(3.3) as $s \to 0$. (It is understood that $R_E \to \infty$ in (3.3).) Further, the integral in (4.31) can be explicitly evaluated to yield

$$\int_0^{sx} \Gamma(\xi)\,d\xi$$

$$= \frac{(1 - \rho)}{\sqrt{\rho}} \text{Log}\left[\frac{\sqrt{1 + \rho sx} + \sqrt{\rho(1 + sx)}}{1 + \sqrt{\rho}}\right] + \sqrt{(1 + \rho sx)(1 + sx)} - 1. \tag{4.33}$$

It may be directly verified that (4.33) satisfies (4.32). Observe that the geometrical optics solution (4.31) preserves the property associated with the exact solution (4.12) that $\phi(-1/s, t) = 0$.

The geometrical optics solution (4.31), of course, describes, within the context of $0 < s \ll 1$, a 'slowly' spatially modulated normal mode. However, even for moderate values of s, (4.31) provides a very good approximation to the exact solution (4.12). Figure 14 is a graph of $\phi(x, 0)$ versus x as determined by the geometrical optics solution (4.31) for exactly the same parameter values as in figure 13 (in particular note that $s = 0.4$). Qualitatively, figure 14 is very similar to figure 13. The only germane difference is that the wavelength of the oscillations in figure 14 is slightly less than those in figure 13.
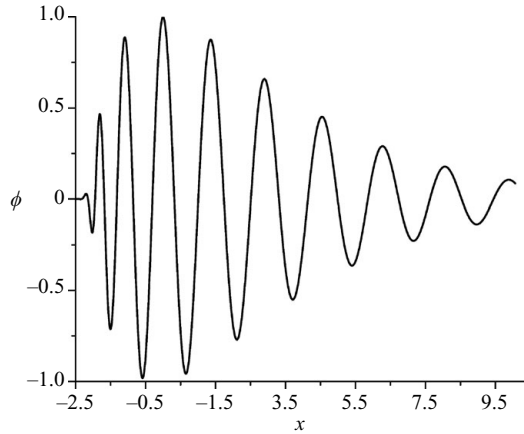
FIGURE 14. Graph of $\phi(x, 0)$ versus x for $x \in (-1/s, -1/s + 20\pi/k)$ as determined by the geometrical optics solution (4.31) with the same parameter values as in figure 13 and $A = 1$. Dimensionally, 1 unit along the x-axis corresponds to about 15 km.

5. Conclusions

The flow of grounded dense water over deep topographic sills is a source point for the formation of many of the ocean currents that comprise the abyssal portion of the thermohaline circulation. The mixing and transport characteristics of these currents determines many aspect of the variability associated with the convective overturning of the oceans and hence climate change. Observations show that these vertically sheared flows can have flow speeds faster than the ambient long internal gravity waves and that in the near-sill region the dynamics are principally governed by a balance between downslope gravitational acceleration and bottom friction. These dynamics suggest the possibility that these overflows can transition to instability through a mixed bottom-friction–Kelvin–Helmholtz destabilization mechanism. The principal purpose of this paper has been to develop a theory for this mixed instability.

In order to study this transition a two-layer model was introduced that allows for the coupling of bottom-intensified roll waves and internal gravity waves over sloping topography. These equations were non-dimensionalized based on classical internal wave scalings. The stability characteristics were thusly described as functions of the bottom drag coefficient and slope, Froude, bulk Richardson and Reynolds numbers and the fractional thickness of the abyssal current to the mean depth of the overlying water column (denoted by δ).

In the limit in which the upper layer mean depth was held constant, normal mode solutions were obtained. In the abyssal layer the instabilities correspond to baroclinic roll waves, and in the overlying water column amplifying internal gravity waves are generated. Several general stability properties were explicitly obtained, including the marginal stability boundary in the (δ, F)-plane. As well, the boundary in the (δ, F)-plane, separating the parameter regimes in which the most unstable mode has a finite or infinite wavenumber was determined. In addition, when it exists, a high-wavenumber cutoff was explicitly determined. Conditions for the possible development of an ultraviolet catastrophe were determined. The growth rate, wavenumber, co-moving and geostationary frequency and the phase velocity of the most unstable mode in the (δ, F)-plane were described.

In the infinite-Reynolds-number limit, an exact solution was obtained which fully includes the effects of mean depth variations in the overlying water column associated with a sloping bottom. The small bottom slope and δ limits of the exact solution were shown to reduce to the normal mode results previously obtained. However, abyssal overflows in the real ocean are expected to never possess the property that the mean depth of the overlying water column is near zero. This in turn suggested the possibility that the general stability problem could be accurately solved using a geometrical optics approximation associated with an underlying (stable or unstable) normal mode. This solution was obtained and compared with the exact solution. As expected, the agreement was very good.

Finally, in summary, for parameter values characteristic of the Denmark Strait overflow, the most unstable mode associated with the mixed instability mechanism described here has wavelength of about 19 km, a geostationary period of about 14 hours, an e-folding amplification time of about 2 hours and a downslope phase speed of about 74 cm s^{-1}.

REFERENCES

ABRAMOWITZ, M. & STEGUN, I. A. 1970 *Handbook of Mathematical Functions*, 9th ed., Dover.

BAINES, P. G. 1984 A unified description of two-layer flow over topography. *J. Fluid Mech.* **146**, 127–167.

BAINES, P. G. 1995 *Topographic Effects in Stratified Flows*. Cambridge University Press.

BALMFORTH, N. J. & MANDRE, S. 2004 Dynamics of roll waves. *J. Fluid Mech.* **514**, 1–33.

BRUCE, J. G. 1995 Eddies southwest of Denmark Strait. *Deep-Sea Res.* **42**, 13–29.

CENEDESE, C., WHITEHEAD, J. A., ASCARELLI, T. A. & OHIWA, M. 2004 A dense current flowing down a sloping bottom in a rotating fluid. *J. Phys. Oceanogr.* **34**, 188–203.

DEWAR, W. K. 1987 Ventilating warm rings. *J. Phys. Oceanogr.* **17**, 2219-2231.

DICKSON, R. R. & BROWN, J. 1994 The production of North Atlantic deep water: sources, rates, and pathways. *J. Geophys. Res.* **99**, 12319–12341.

DRAZIN, P. G. & REID, W. H. 1981 *Hydrodynamic Stability*. Cambridge University Press.

EMMS, P. W. 1998 A streamtube model of rotating turbidity currents. *J. Mar. Res.* **56**, 41–74.

GIRTON, J. B. & SANFORD, T. B. 2001 Synoptic sections of the Denmark Strait overflow. *Geophys. Res. Lett.* **28**, 1619–1622.

GIRTON, J. B. & SANFORD, T. B. 2003 Descent and modification of the Denmark Strait overflow. *J. Phys. Oceanogr.* **33**, 1351–1364.

HOUGHTON, R. W., SCHLITZ, R., BEARDSLEY, R. C., BUTMAN, B. & CHAMBERLIN, J. L. 1982 The middle Atlantic bight cold pool: evolution of the temperature structure during summer 1979. *J. Phys. Oceanogr.* **12**, 1019–1029.

JEFFREYS, H. 1925 The flow of water in an inclined channel of rectangular bottom. *Phil. Mag.* **49**, 793–807.

JIANG, L. & GARWOOD, R. W. 1996 Three-dimensional simulations of overflows on continental slopes. *J. Phys. Oceanogr.* **26**, 1214–1233.

JUNGCLAUS, J. H., HAUSER, J. & KÄSE, R. H. 2001 Cyclogenesis in the Denmark Strait overflow plume. *J. Phys. Oceanogr.* **31**, 3214–3228.

KARSTEN, R. H., SWATERS, G. E. & THOMSON, R. E. 1995 Stability characteristics of deep water replacement in the Strait of Georgia. *J. Phys. Oceanogr.* **25**, 2391–2403.

KÄSE, R. H., GIRTON, J. B. & SANFORD, T. B. 2003 Structure and variability of the Denmark Strait overflow: model and observations. *J. Geophys. Res.* **108** (C6), 10.1029/2002JC001548.

KÄSE, R. H. & OSCHLIES, A. 2000 Flow through Denmark Strait. *J. Geophys. Res.* **105**, 28527–28546.

KILLWORTH, P. D. 1977 Mixing on the Weddell Sea continental slope. *Deep-Sea Res.* **24**, 427–448.

KRAUSS, W. & KÄSE, R. H. 1998 Eddy formation in the Denmark Strait overflow. *J. Geophys. Res.* **103**, 15523–15538.

LEBLOND, P. H., MA, H., DOHERTY, F. & POND, S. 1991 Deep and intermediate water replacement in the Strait of Georgia. *Atmos.-Ocean* **29**, 288–312.

LEBLOND, P. H. & MYSAK, L. A. 1978 *Waves in the Ocean.* Elsevier.

LYAPIDEVSKII, V. YU. 2000 The structure of roll waves in two layer flows. *J. Appl. Maths. Mech.* **64**, 937–943.

MASSON, D. 2002 Deep water renewal in the Strait of Georgia. *Estuarine Coast. Shelf Sci.* **54**, 115–126.

PEDLOSKY, J. 1987 *Geophysical Fluid Dynamics.* Elsevier.

PRICE, J. F. & BARINGER, O. M. 1994 Outflows and deep water production by marginal seas. *Progr. Oceanogr.* **33**, 161–200.

RESZKA, M. K., SWATERS, G. E. & SUTHERLAND, B. R. 2002 Instability of abyssal currents in a continuously stratified ocean with bottom topography. *J. Phys. Oceanogr.* **32**, 3528–3550.

SMITH, P. C. 1975 A streamtube model for bottom boundary currents in the ocean. *Deep-Sea Res.* **22**, 853–873.

SPALL, M. A. & PRICE, J. F. 1998 Mesoscale variability in Denmark Strait: the PV outflow hypothesis. *J. Phys. Oceanogr.* **28**, 1598–1623.

SUTYRIN, G. G. 2007 Ageostrophic instabilities in a horizontally uniform flow along a slope. *J. Fluid Mech.* **588**, 463–473.

SWATERS, G. E. 1991 On the baroclinic instability of cold-core coupled density fronts on a sloping continental shelf. *J. Fluid Mech.* **224**, 361–382.

SWATERS, G. E. 1998 Numerical simulations of the baroclinic dynamics of density-driven coupled fronts and eddies on a sloping bottom. *J. Geophys. Res.* **103**, 2945–2961.

SWATERS, G. E. 2003 Baroclinic characteristics of frictionally destabilized abyssal overflows. *J. Fluid Mech.* **489**, 349–379.

SWATERS, G. E. 2006a On the frictional destabilization of abyssal overflows dynamically coupled to internal gravity waves. *Geophys. Astrophys. Fluid Dyn.* **100**, 1–24.

SWATERS, G. E. 2006b The meridional flow of source-driven abyssal currents in a stratified basin with topography. Part I. Model development and dynamical characteristics. *J. Phys. Oceanogr.* **36**, 335–355.

SWATERS, G. E. 2006c The meridional flow of source-driven abyssal currents in a stratified basin with topography. Part II. Numerical Simulation. *J. Phys. Oceanogr.* **36**, 356–375.

SWATERS, G. E. & FLIERL, G. R. 1991 Dynamics of ventilated coherent cold eddies on a sloping bottom. *J. Fluid Mech.* **223**, 565–587.

WHITHAM, G. B. 1974 *Linear and Nonlinear Waves.* Wiley.

WORTHINGTON, L. V. 1969 An attempt to measure the volume transport of Norwegian Sea overflow water through the Denmark Strait. *Deep-Sea Res.* **16**, 421–432.

WORTHINGTON, L. V. & WRIGHT, W. R. 1970 *North Atlantic Ocean Atlas,* vol. 2. The Woods Hole Oceanographic Institution.